

Article

Computational Studies of Air-Mist Spray Cooling in Continuous Casting

Vitalis Anisiuba, Haibo Ma, Armin Silaen and Chenn Zhou *

Center for Innovation through Visualization and Simulation (CIVS), Purdue University Northwest, Hammond, IN 46323, USA; vanisiub@pnw.edu (V.A.); ma344@pnw.edu (H.M.); asilaen@pnw.edu (A.S.)

* Correspondence: czhou@pnw.edu

Abstract: Due to the significant reduction in water droplet size caused by the strong air-water interaction in the spray nozzle, air-mist spray is one of the promising technologies for achieving high-rate heat transfer. This study numerically analyzed air-mist spray produced by a flat-fan atomizer using three-dimensional computational fluid dynamics simulations, and a multivariable linear regression was used to develop a correlation to predict the heat transfer coefficient using the casting operating conditions such as air-pressure, water flow rate, casting speed, and standoff distance. A four-step simulation approach was used to simulate the air-mist spray cooling capturing the turbulence and mixing of the two fluids in the nozzle, droplet formation, droplet transport and impingement heat transfer. Validations were made on the droplet size and on the VOF-DPM model which were in good agreement with experimental results. A 33% increase in air pressure increases the lumped HTC by $3.09 \pm 2.07\%$ depending on the other casting parameters while an 85% increase in water flow rate reduces the lumped HTC by $4.61 \pm 2.57\%$. For casting speed, a 6.5% decrease in casting speed results in a $1.78 \pm 1.42\%$ increase in the lumped HTC. The results from this study would provide useful information in the continuous casting operations and optimization.

Keywords: air-mist spray; atomization; continuous casting; impingement cooling; heat transfer coefficient



Citation: Anisiuba, V.; Ma, H.; Silaen, A.; Zhou, C. Computational Studies of Air-Mist Spray Cooling in Continuous Casting. *Energies* **2021**, *14*, 7339. <https://doi.org/10.3390/en14217339>

Academic Editors: Eusebio Valero and Javier de Vicente

Received: 12 October 2021
Accepted: 2 November 2021
Published: 4 November 2021

Publisher's Note: MDPI stays neutral with regard to jurisdictional claims in published maps and institutional affiliations.



Copyright: © 2021 by the authors. Licensee MDPI, Basel, Switzerland. This article is an open access article distributed under the terms and conditions of the Creative Commons Attribution (CC BY) license (<https://creativecommons.org/licenses/by/4.0/>).

1. Introduction

Secondary cooling is critical in the continuous casting process, which was introduced in the late 1950s and is now used to produce more than 90% of the steel in the world [1,2]. In 2009, global crude steel production exceeded 1220 million tons, with continuously cast steel accounting for 92 percent of total output. [3] As a result, given that spray cooling is critical to this process, its importance in this, as well as many other applications in which it participates, is obvious. At around 1473 K (1200 °C), a solidified shell in steel CC exits the mold or primary cooling system and enters a containment-spray cooling arrangement known as the secondary cooling system, which is made of closely spaced support rolls, between which nozzles are interspaced to achieve a spray cooling pattern that ensures the strand solidifies completely through its thickness before it reaches the system exit. Spray cooling accounts for approximately 60% of the heat extracted through the secondary cooling system of CC machines (i.e., direct spray impingement, roll contact, radiation, and convection to draining water) [4] but this contribution can be much larger in its upper zones [5,6].

In secondary cooling zones, the solidified shell is subjected to large temperature changes on its surface, which can result in complex phase transformation and residual stress inside the slab. As a result, uniform rapid heat removal from the slab is desired, while slab cracking and deformation are avoided. The mechanisms of spray cooling during the continuous casting process are complex, but certain fundamental phenomena, such as atomization of water droplets through spray nozzles, droplet wall impingement and heat transfer, and evaporation of water droplets during or after the impingement heat transfer, have

been identified by researchers over the past decades. These topics are further subdivided into two major categories: spray and impinging heat transfer. [7]. Many experimental procedures for measuring the heat transfer coefficient (HTC) across the slab surface as one of the parameters to quantify heat transfer rate [8–12] have been developed. Understanding HTC distribution on slab surfaces is critical because it is a transitional parameter between spray cooling and solidification. The HTC can be viewed as the result of spray cooling, but it also serves as a predictor of liquid steel solidification. Understanding the HTC distribution gives you a unique perspective on spray adjustment and slab quality control. However, measuring HTC directly on the slab surface is nearly impossible because the slab is constantly moving, has an average temperature of more than 1000 K, and the liquid steel inside the solid shell is dynamically solidifying [7]. HTC is also a localized parameter whose value is affected by both spray characteristics and slab surface conditions, namely water flow rate, air pressure, standoff distance, nozzle to nozzle distance, and slab temperature [13]. As a result, a massive number of experiments would be required to generate correlations for each type of nozzle at different operating conditions.

Many studies [14–18] on the air mist spray cooling process above the Leidenfrost temperature have been conducted to estimate the heat transfer coefficient, but they are frequently inapplicable to cooling situations that differ from the experimental conditions. A specific class of heat transfer coefficient models assumes the heat transfer coefficient as a function of the water flux w ($L \text{ min}^{-1} \text{ m}^{-2}$), droplet diameter d (m), and jet velocity v . (m s^{-1}),

$$h = f(d, v)w^b \quad (1)$$

Although it was reported in [15,16] that the jet velocity does not influence the spray cooling heat transfer significantly.

A steady state method based on induction heating was developed for measuring the local heat flux q under practical air-mist cooling conditions, generated with different pneumatic nozzles, and the following expression was obtained [19]:

$$-q = 0.307w^{0.319}u_{z,v}^{0.317}T_w^{0.144}d_{30}^{-0.036} \quad (2)$$

The author also developed a correlation to predict the heat transfer coefficient as:

$$h = 379.93w^{0.318}u_{z,v}^{0.330}T_w^{-0.895}d_{30}^{-0.024} \quad (3)$$

When the wall temperature T_w is between 723 K and 1453 K, which corresponds to the film boiling regime, it has been demonstrated that q increases with increasing drop velocity, water impact flux, slab surface temperature, and drop diameter, and that q decreases with decreasing drop diameter [20]. The impacting droplets of water spray will only come into touch with the surface for a brief amount of time during the film boiling regime; yet, the heat transfer that results is significant [21]. Convection in the layer of vapor beneath the droplet-surface contact is one of the heat transfer mechanisms that occur at the contact point between the two droplets. The heat transmission from the surface of the drops is accompanied by radiative heat transfer from the surface and convection heat transfer from flowing air on the surfaces. Due to the droplet-surface interactions, the heat transfer is also influenced by the material characteristics and roughness of the surface. For steel surfaces, it was discovered in a study [22] that the surface heat flux maintains within the range of 0.5 MW/m^2 even when the film boiling regime is employed. The heat flux at the onset of transition boiling regime, i.e., at the minimal film boiling heat flux, was also reported in [23], and it was found to be in the range of 0.43 MW/m^2 with a steel surface at $500 \text{ }^\circ\text{C}$ as an initial temperature.

The key physics in dispersed multiphase flows are in the mass, momentum, and energy coupling between the phases. In dispersed multiphase flows, the evolution of the interface between the phases is considered of secondary importance. Processes such as droplet or bubble break-up and agglomeration do indeed alter the interface between

the phases. However, in the context of dispersed multiphase flows, one accounts for the interface between the dispersed and carrier phases in terms of particle-size spectra without considering the detailed evolution of the interface [24]. Particle-laden turbulent flows can be broadly categorized into dilute and dense regimes, depending on the dispersed phase volume fraction [25]. In dilute flows, the particle motion is primarily dominated by the fluid drag and lift forces, and inter-particle collisions are negligible. On the other hand, in dense flows the particle motion is controlled by collisions or continuous contact. The fractional volume occupied by the dispersed phase (Φ_v) and the mass loading (Φ_m), defined as the ratio of mass of the dispersed to carrier phase, are two critical parameters that determine the level of interaction between the phases. When Φ_v and Φ_m are small, the dominant effect is that of the turbulent carrier flow on the dynamics of the dispersed phase (i.e., one-way coupled). When the mass of the dispersed phase is comparable with that of the carrier phase, the back influence of the dispersed phase on the carrier-phase dynamics cannot be ignored (i.e., two-way coupled). Finally, when Φ_v increases, interactions between particles (such as collision, agglomeration, and break-up) become important, and this regime is described as four-way coupled [26,27]. One of the key features of particle distribution in turbulent flows is the phenomenon of preferential accumulation [28–30]. It is now well accepted that even in isotropic turbulence, particle distribution is not uniform. Heavier-than-fluid particles tend to accumulate in regions of high strain rate and avoid regions of intense vorticity. In contrast, lighter-than-fluid particles (or bubbles) tend to congregate in vortical regions. Furthermore, when the particle Reynolds number increases above a few hundred, the effect of vortex shedding introduces a stochastic component to interphase coupling.

The motion of inertial particle pairs can differ substantially depending upon whether the two particles have the same (monodisperse) or different (bidisperse) inertia. The dispersion of spray drops in a gas is important in order to bring about efficient mass and heat transfer between liquid and gas phases. Particle accelerations play a key role in the relative motion of bidisperse particles and the authors in [31] found that reducing Froude number (Fr) leads to an enhancement of the accelerations but a suppression of their intermittency while for monodisperse case, decreasing the Fr leads to a uniform suppression of the inertial particle relative velocities in all directions [32,33]. Particle inertia can be characterized by the Stokes number, $St = \tau_p / \tau_\eta$, where τ_p is the particle response time, τ_η is the flow time scale, and can also be expressed as $St = (1/18)[(\rho_p - \rho_f) / \rho_f](d/\eta)^2$ where η is the Kolmogorov scale, d is the particle diameter, ϵ is the mean turbulent kinetic energy dissipation rate, ρ_p and ρ_f are the particle and fluid density. The effect of gravity on the flow can be characterized by the Froude number, $Fr = a_\eta / g = \epsilon^{3/4} / (\nu^{1/4} g)$, where $a_\eta = u_\eta / \tau_\eta$ is the Kolmogorov acceleration [31,32]. It has been found that bidispersity alone enhances the particle relative velocities, and these relative velocities are further enhanced by gravity [34–37]. For Stokes numbers $St > 1$, the effect of Reynolds number R_λ on the accelerations is enhanced by gravity, since settling causes the particle accelerations to be affected by a larger range of flow scales. Gravity not only leads to finite settling velocities for inertial particles, but it also modifies the way the particles interact with the turbulent flow [29,38]. In the presence of gravity, the particles fall through the flow, and the timescale of particle relative velocity is reduced compared to the case without gravity [33]. In the regime $Fr \ll 1$ and $St \geq O(1)$, gravity significantly enhances the particle displacement over the time span due to the fast settling of the particles [31,34]. However, when $|\Delta St| \ll 1$, gravity suppresses the relative dispersion as the settling velocity contribution is small, and gravity suppresses the nonlocal contribution to the particle dynamics [31,34]. For $Fr = \infty$, increasing St monotonically decreases the particle accelerations due to the effect of preferential sampling, whereby the inertial particles avoid strongly vortical regions where there is rapid fluid acceleration, and due to the filtering effect, whereby with increasing St , the particles become sluggish and have a modulated response to the fluid accelerations along their trajectory [39,40]. DNS was used by [41] to study the dispersion of bidisperse particles with and without gravity and found that the differential settling velocities of the

particles leads to faster relative dispersion of bidisperse particles as compared to those dispersing in the absence of gravity.

Basically, air-water mist is a suspension of very small droplets of water in an air jet that is created as a result of liquid shearing and then atomization caused by pressured air jet impingement on the margin of the liquid opening. For quenching metal plates in research and development, air-atomized spray is becoming increasingly popular due to its ability to extract more heat from the plate in a shorter period of time [42]. It is possible for air-mist atomizers to shatter a liquid jet or sheet into ligaments and then droplets by utilizing the kinetic energy of a flowing airstream [43]. Since the late 1970s, there has been a lot of discussion on air-mist heat extraction studies. When compared to spray—hydraulic—nozzles, the wide range of cooling conditions [44,45], from mild to intense, as well as the low proclivity to clogging, have been underlined as advantages of air-mist—pneumatic—nozzles. This is owing to the huge turndown ratio (the ratio between the minimum and maximum water flow) and the controllability of the air/water volumetric ratios [21], both of which are important factors. Furthermore, it was asserted that air-mist nozzles, rather than hydraulic nozzles, resulted in fewer longitudinal cracks than hydraulic nozzles because they reduced changes in slab surface temperature [46]. In experiments with the same water flow rate, mist cooling was found to have a higher heat transfer coefficient than spray cooling [45,46], as would be expected given that mist cooling involves the application of a pressure that modifies the characteristics of water droplets, resulting in more intense mist cooling. Fine droplets are produced by air mist nozzles, and evaporation is the primary source of their cooling effect. This type of nozzle has a wide range of controllability, and the intensity of the cooling can be changed by varying the air and water pressures [47]. It is possible for them to deliver spray droplets within their own generated gas flow fields at high velocities when compared to conventional hydraulic systems. Furthermore, the drop size produced by them is often significantly smaller than that produced by basic hydraulic atomizers [48]. Air mist nozzles with flat jets, such as the one employed in this study, have been effectively used for secondary cooling purposes in continuous steel casting production for more than fifteen years. [49,50] It has been reported that the heat transfer coefficient is directly proportional to both the droplet diameter and the initial collision velocity, and that this is indicative of the significant relationship between the heat-transfer process and the droplet-deformation behavior during impact [51]. According to consensus [51,52], the Weber number linked with the normal-collision velocity is the most accurate way to characterize the impact or deformation mode of the drops.

When air pressure is increased in the range of 200 to 400 kPa, it is hypothesized that the effect on heat extraction is due to the effect on the droplet size and velocity, with the hypothesis being that small droplets with high momentum are better suited to penetrate the vapor layer and reach the hot surface when compared to drops produced by hydraulic nozzles. However, the authors [53] asserted that the effect of air pressure decreased as water impact flux increased, such that sprays and air-mists produced cooling results that were comparable; their study included water impact flux ranging from 0.68 to 2.72 L/m²s and included sprays and air-mists produced cooling results that were similar. On the other hand, the researchers at [54] and [55] found that for a given water impact flow (in the range of 0.2 to 16 L/m²s), the heat transfer coefficient increases as the air nozzle pressure increases. In their study, the scientists found that increasing the air flow rate to the water flow rate ratio results in finer and quicker droplets that contact the surface more quickly. It has been discovered in other studies [54,56–58] using air-mist nozzles that an increase in air pressure at a constant water flow rate causes an increase in boiling convection heat flux as a result of changes in spray parameters; however, no correlations between these parameters and heat transfer coefficient have been established. It should be noted that the drop size and velocity utilized to interpret the heat transfer results in the investigations [15,17,59] were measured in the absence of a hot surface and were therefore different from one another. A decrease in the volume (and number) of droplets with sufficient inertia was observed with an increase in water flow rate while maintaining constant air pressure. The diameter

of the drops generated became larger and their velocities became smaller in general as the water flow rate increased at constant air pressure. It was asserted that drops with a median diameter between 100 and 200 μm were ideal, and that drop diameter was the second most relevant mist parameter on heat extraction after water impact flux [54] following drop diameter. For efficient heat extraction, the authors asserted that larger droplets would only partially evaporate and leave a large portion of liquid on the surface, whereas smaller drops would be unable to penetrate the vapor layer and reach the surface. They recommended a compromise between droplet diameter and droplet velocity in order to achieve efficient heat extraction on the surface. When it comes to heat transfer above leidenfrost temperature, that is, when it comes to within the film boiling regime, it was discovered in [56] that the parameter controlling heat transfer intensity was the kinetic energy of droplets, which was shown to be affected by air pressure. Furthermore, according to another study [18], heat transmission is regulated not only by water impact flow but also by droplet diameter and droplet velocity, all of which are major factors.

Since the introduction of the continuous casting process, various enhancements have been made to the secondary cooling area of the furnace. Using computational fluid dynamics (CFD) to build an accurate model that correlates varying nozzle settings with the heat transfer coefficient (HTC) over the surface of the slabs, the spray cooling control will be improved in the secondary cooling phase of the reactor. There are currently no models that can do this for air-mist spray cooling, and in order to obtain the correlation, the nozzles must be sent out for experimental testing, which can take several weeks to complete. If a model could produce the same results in a fraction of the time, this would be a huge breakthrough because it would reduce the amount of time spent waiting for the results and eliminate the need to outsource the testing of the nozzles.

Some critical characteristics, such as casting speed and standoff distance, are not included in the correlations presented thus far. Changing the casting speed can change the droplet residence time on the steel surface, resulting in an increase or decrease in the amount of energy transferred [60]. A direct correlation between casting velocity and heat transfer coefficient was suggested [47], stating that the motion of the hot surface affected the flow of liquid on it as well as the generation of vapor in front and behind the impinging jet. However, no evidence for this claim was offered. Their conclusion was that the cooling intensity does not remain constant when the casting speed is changed. When CC is modelled for design or control purposes, they discovered that the velocity of motion of the cooled surface is still another variable that must be considered. Reduced orifice-to-surface distance (standoff distance) increased the magnitude of volumetric flux, which has been reported in comparative work between steel and aluminum [61]. This has been shown to hasten the onset of the rapid cooling stages of the quench while also improving overall cooling efficacy. The investigation of the influence of nozzle-to-surface distance on heat transfer during spray cooling of brass and Inconel [62] revealed that as the nozzle-to-surface distance increases, the heat transfer coefficient decreases more slowly, with the rate of decrease being determined mostly by the water flux of the spraying system. Therefore, it is required to construct a more thorough and general HTC correlation in order to incorporate these events into the model.

One possibility is to use a numerical method to quantify HTC on the slab surface in a localized area. CFD has developed into a strong tool and has achieved widespread acceptance for its ability to solve complex fluid flow and heat transfer problems in a reasonable amount of time, thanks to the advancements in high-performance computing technology. Despite this, only a few good numerical models of spray cooling and solidification during secondary cooling have been recorded, owing to the intricate physical phenomena involved. Development of a complete numerical model that can be utilized to forecast spray pattern and associated heat transfer during the secondary cooling process is crucial [63].

A new methodology for numerically modeling air mist spray cooling and developing HTC correlation for continuous steel casting is proposed in this study. A four-step 3-D CFD

simulation approach is used to model droplet formation, transport, and impingement heat transfer with an air mist spray cooling. To create a database for HTC correlation, various casting conditions are simulated. To predict lumped HTC at different casting conditions, a multivariable regression analysis was used to generate a simple mathematical correlation. This would aid in dynamic control and parameter optimization for continuous casting.

2. Methodology

Since the densities and dynamic viscosities of the two fluids of concern, air and water, are 0.00123 and 0.0178, respectively, it is assumed that they are incompressible. For a variety of reasons, a four-step simulation technique was adopted. It is first necessary to create a simulation of internal flow in the nozzle, in order to accurately depict the mixing and turbulence phenomena that occur between air and water within the nozzle. The spraying system co. flat fan nozzle with a spray angle of 90° is employed in this simulation. For this reason, a very tiny cell size is chosen to capture the majority of the phenomena occurring between the point of jet exit from the nozzle and the impingement and cooling of the steel slab, which results in a very long computational time to run just once for the nozzle-to-surface distance. Furthermore, the VOF to DPM approach in ANSYS (ANSYS Inc., Pittsburgh, PA, USA) Fluent was tested by running the entire spray domain at once and was found to be successful in converting the liquid phase into droplets; however, the number of droplets produced was very small and the computational time was too high, leading to the use of an alternative method of droplets size distribution (Nukiyama-Tanasawa) [64] to generate the droplets in STAR CCM+ (Siemens Digital Industries Software, Plano, TX, USA) CFD software to generate the droplets.

Illustration of the simulation approach and the most critical physics in the spray cooling process is shown in Figure 1. For modeling the development and breakup of jets [65–68], the Eulerian–Eulerian technique has gained popularity numerically. As a result of the tight interaction between the liquid jet and the surrounding air, this method can be time-consuming and mathematically complex. When the region of interest is located further downstream, many scholars have chosen for the Eulerian–Lagrangian technique as an alternative strategy. When the primary and secondary breakups are ignored, the initial spray characteristics are defined at the breakup length, at which point the liquid jet has entirely broken down into droplets [69]. Due to its lower processing cost when compared to the Eulerian–Eulerian technique, the Eulerian–Lagrangian method is used. The entrainment of air caused by the high-speed water spray is represented in the Eulerian frame, whereas water droplets are considered as discrete phases and tracked in the Lagrangian frame, respectively.

2.1. Continuous Phase (Air)

The motion of the air phase was described in a Eulerian frame of reference according to the following equations.

Continuity equation:

$$\frac{\partial \rho_{\text{air}}}{\partial t} + \nabla \cdot (\rho_{\text{air}} \mathbf{u}_{\text{air}}) = 0 \quad (4)$$

where ρ_{air} is the air density, and \mathbf{u}_{air} is the air velocity.

Momentum equation:

$$\frac{\partial}{\partial t} (\rho_{\text{air}} \mathbf{u}_{\text{air}}) + \nabla \cdot (\rho_{\text{air}} \mathbf{u}_{\text{air}}^2) = -\nabla P + \nabla \cdot (\mu_{\text{air}} \nabla \cdot \mathbf{u}_{\text{air}}) + \rho_{\text{air}} \mathbf{g} + S_{\text{air-drop}} \quad (5)$$

where $S_{\text{air-drop}}$ is the source-term coupling the momentum of the air with that of the drops according to the following expression:

$$S_i = \frac{\pi}{6\rho_{\text{vcell}}} \sum \dot{n} \left(\rho_{\text{drop}}^{\text{out}} u_i^{\text{out}} (d_{\text{drop}}^{\text{out}})^3 \right) - \rho_{\text{drop}}^{\text{in}} u_i^{\text{in}} (d_{\text{drop}}^{\text{in}})^3 \quad (6)$$

which establishes, according to the particle source in cell model [70], that the momentum transferred between the air and the drops in a given cell of the fixed Eulerian grid is equal to the change in the momentum of all the drops, g , passing through it over the Lagrangian time-step.

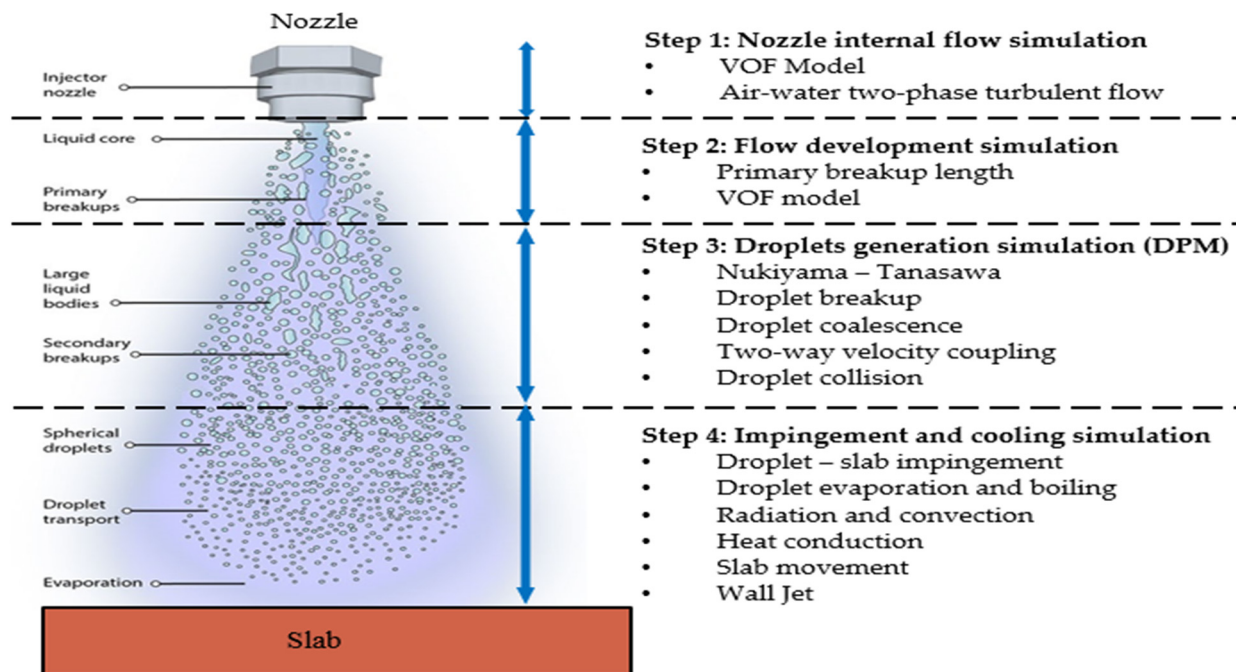


Figure 1. Simulation methodology, physics and CFD models of spray cooling. <http://www.spray-imaging.com/spray-description.html> (accessed on 10 June 2021).

The majority of impinging jets used in industry produce turbulent flow as a result of the development of vortices along the sides of the jet, which is analogous to the Kelvin-Helmholtz instability. Accurately anticipating the presence of turbulence is extremely difficult, and it is not always possible. In accordance with the extensive comparisons made by [71], Menter's Shear Stress Transport (SST) model [72] is one of the most suited turbulence models for predicting impinging jet flow in terms of accuracy while not requiring excessive processing capacity. The SST model combines the k - ω model near the wall, which requires a finely spaced mesh near the wall to generate accurate results, and the k - ϵ model farther from the wall in order to take advantage of the strengths of each model in order to maximize the accuracy of the results.

2.2. Multiphase Flows

The precise identification of interface dynamics, which allows flow regimes to be established and associated inter-phase transfer processes to be quantified, is critical to the numerical simulation of multiphase flows. This is the foundation of numerical simulation of multiphase flows. Interpenetrating-continua technique, also known as the two-fluid method [73], is used to describe phenomena occurring at the interface between separating phases. Direct interface tracking methods, on the other hand, are used to directly mimic topology and dynamics of the interface [74]. (ITM). Each point in the mixture is occupied simultaneously (in variable proportions) by both phases in the averaged two-fluid formalism, therefore distinct conservation equations are required for each field in the formalism. For predicting specific kinds of multiphase flows, the volume of fluid (VOF) approach is one of the most often applied Eulerian-based ITMs [74–77], and it is shown to be effective. The VOF approach relies on the definition of the liquid volume-fraction field

or the volumetric proportion occupied by one of the phases within volume V . This fluid property is conventionally denoted (in a discrete form) by F_{ij} and defined by:

$$F_{ij} = \frac{1}{V_{\text{cell } V}} \chi(x, t) dV \quad (7)$$

where χ is a composition field. Equation (7), therefore, represents the evolution of the liquid volume-fraction, identifying flow regions containing pure liquid (where $F_{ij} = 1$) from pure gas flow regions (where $F_{ij} = 0$). Interfacial cells are such that $0 < F_{ij} < 1$.

2.3. Atomization

To put it simply, atomization is the act of breaking up a continuous liquid into hundreds or thousands of droplets, resulting in an increase in the surface area of the liquid. Therefore, atomization improves the efficiency of all processes related with surface phenomena as a result of its effect on their efficiency. Droplets are created physically as a result of two sequential breakup processes, namely, the breakup of the liquid sheet and the breakage of the ligaments. This is determined by the hydrodynamics within the atomizer and the disintegration of the liquid sheet, and it is classically represented by the size and velocity distributions of the droplets within the spray stream. Combined, the two breakup processes are referred to as primary breakup, as opposed to secondary breakup, in which the droplets formed as a result of the primary breakup process further break up into smaller droplets as a result of aerodynamic instabilities or droplet-droplet collisions (see Figure 1). It is well-known that the main split is a well-studied process, and the relevant hypotheses have been extensively tested in recent decades [78–82].

Depending on the operating flow conditions of the atomizer, the liquid jet is subjected to various instabilities including capillary, helical, Kelvin–Helmholtz (KH) instability, etc. and different mechanisms of breakup of the liquid core and ligaments have been identified in the earlier works. Some researchers conducted experimental studies and proposed empirical correlations to evaluate the primary breakup length for air-blast nozzles [83–87]. In this study, the breakup length was estimated as [83]:

$$\frac{L}{D_1} = 0.66 We_g^{-0.4} Re_1^{0.6} \quad (8)$$

2.4. Droplet Coalescence and Breakup

The droplet coalescence model is based on the O'Rourke method [88], which involves stochastic collision estimation. The WAVE breakup model is used to account for droplet breakup caused by the relative velocity between the droplet and the surrounding air. The model assumes that a droplet's breakup time and resulting child droplet size are determined by the fastest-growing Kelvin-Helmholtz instability:

$$\frac{dr_{\text{parent}}}{dt} = \frac{\Lambda \Omega (r_{\text{parent}} - r_{\text{child}})}{3.726 B_1 \Gamma_{\text{parent}}} \quad (9)$$

2.5. Droplet Motion and Convective Heat Transfer

The Lagrangian method was used to model the motion of the drops. Their motion equation, which followed Newton's law, took into account aerodynamic drag and gravity force and was expressed as follows:

$$\frac{du_{\text{drop}}}{dt} = \frac{3\mu_{\text{drop}} C_D Re_{\text{drop}}}{4\rho_{\text{drop}} d_{\text{drop}}^2} (u_{\text{air}} - u_{\text{drop}}) + \frac{g(\rho_{\text{drop}} - \rho_{\text{air}})}{\rho_{\text{drop}}} \quad (10)$$

The air-droplet interaction is represented by the drag force term, and the drag coefficient, C_D , can be calculated using the piecewise function in [89]. Other aerodynamic

forces that could affect droplet motion (namely the pressure gradient, virtual mass, and the Basset term) were ignored because they are on the order of the gas-droplet density ratio, [73], which is 10^{-3} in this case. Furthermore, the Saffman lift and Magnus forces were ignored because the drops are not in a high-shear region of the flow field for the majority of the flow field; [73] this was justified because the motion of the drops in the vicinity of the impact plane was not analyzed in the current article. Droplet trajectories are computed separately at specific intervals during the continuous phase iterations. The trajectory of the drops was computed from the change of their position-vector components with time as follows:

$$\frac{dx_{\text{drop}}}{dt} = u_{\text{drop}} \quad (11)$$

Air-droplet interaction is modeled via the drag force term, which is added to the momentum equation of air as a source.

Droplet temperature changes during the spray cooling process are computed from the following energy balance equation of a droplet:

$$m_{\text{drop}} c_p \frac{dT_{\text{drop}}}{dt} = \pi d_{\text{drop}}^2 h (T_{\infty} - T_{\text{drop}}) + \frac{dm_{\text{drop}}}{dt} h_{fg} + \pi d_{\text{drop}}^2 \epsilon_{\text{drop}} \sigma_{\text{SB}} (T_{\text{R}}^4 - T_{\text{drop}}^4) \quad (12)$$

The convective heat transfer coefficient h can be obtained by the Ranz-Marshall model [90]. The rate of droplet vaporization is governed by the concentration difference between the surface of droplet and the airstream, and the corresponding mass change rate of the droplet can be calculated from the following:

$$\frac{dm_{\text{drop}}}{dt} = \pi d_{\text{drop}}^2 k_c (C_s - C_{\infty}) \quad (13)$$

The coefficient k_c in Equation (6) can be obtained from the Sherwood number correlation with the similar form as Equation (8):

$$\text{Sh}_{\text{drop}} = \frac{k_c d_{\text{drop}}}{D_{\text{vapour}}} = 2.0 + 0.6 \text{Re}_{\text{drop}}^{0.5} \text{Sc}^{0.33} \quad (14)$$

2.6. Droplet-Wall Impingement Model

The wall jet model developed by Naber and Reitz [91] considers three different outcomes, namely stick, reflect, and wall jet, depending on the properties of each individual incoming droplet. In the stick mode, after impingement, the droplet remains in contact with the wall and continues to vaporize. The normal velocity component of a droplet is changed to the opposite sign in the reflect mode, while the magnitude of both the normal and tangential velocity components remains constant. The model treats the impingement of a continuous stream of closely spaced droplets as an inviscid liquid jet emitted from the stagnation point on the solid surface in the wall jet mode. The analytical solution for an axisymmetric impingement uses the following empirical function for the liquid jet with a height of H as a function of the angle at which the droplet leaves the horizontal impingement:

$$H(\Psi) = H_{\pi} e^{\beta(1 - \frac{\Psi}{\pi})} \quad (15)$$

The probability that a droplet leaves the impingement point at an angle between Ψ and $\Psi + \Delta\Psi$ is given by integrating the expression for $H(\Psi)$:

$$\Psi = -\frac{\pi}{\beta} \ln \left[1 - P \left(1 - e^{-\beta} \right) \right] \quad (16)$$

The expression for β is given as:

$$\sin(\varnothing) = \frac{e^\beta - 1}{(e^\beta - 1) \left(1 + \left(\frac{\pi}{\beta} \right)^2 \right)} \quad (17)$$

2.7. Impingement Heat Transfer Model

Although droplet is assumed to be spherical throughout its lifetime, droplets may deform and remain in direct contact with the solid surface for a brief period of time following an impingement. Based on pure heat conduction, the amount of heat exchanged between the droplet and the solid shell can be calculated as:

$$\frac{d}{dt} (m_{\text{drop}} c_p T_{\text{drop}}) = \frac{k_{\text{drop}} A_{\text{cond}}}{s_{\text{slab}}} (T_{\text{slab}} - T_{\text{drop}}) \quad (18)$$

The expression in [51] is used to calculate the effective droplet-wall contact area, A_{cond} . Throughout the continuous casting process, the slab temperature is higher than the Leidenfrost temperature [92]. Droplet vaporization is applied to predict the vaporization from the discrete phase droplet and is initiated when the temperature of the droplet reaches the vaporization temperature and continues until the droplet reaches the boiling point or until the droplets volatile fraction is completely consumed. Considering the high temperature of the slab, it is assumed that the vaporization rates would be high and so the effect of the convective flow of the evaporating material from the droplet surface to the bulk gas phase becomes important. To this effect, the convective/diffusion-controlled model of [93,94] was used to model the droplet vaporization.

2.8. Slab Movement

In order to model the moving effect of the slab relative to the nozzle, two sets of reference frames were used in the simulations: the stationary reference frame and the moving reference frame. The whole set of governing equations for air and droplets is solved with reference to the stationary reference frame, but the energy equation for the slab in the computational domain is defined with reference to the moving reference frame, as shown below:

$$\frac{\partial}{\partial t} \left(\rho_{\text{steel}} h_{\text{steel}} + \frac{|\bar{u}_r|^2 \rho_{\text{steel}}}{2} \right) + \nabla \cdot \left[\bar{u}_r \left(\rho_{\text{steel}} h_{\text{steel}} + \frac{\bar{u}_r^2 \rho_{\text{steel}}}{2} \right) \right] = \nabla \cdot \left[k_{\text{steel}} \nabla T + \bar{\tau} \bar{u}_r \right] \quad (19)$$

The relative velocity, \bar{u}_r between the two reference frames is defined as:

$$\bar{u}_r = \bar{u}_{\text{stationary}} - \bar{u}_{\text{moving}} \quad (20)$$

2.9. Simulation Approach

2.9.1. Section 1 (Internal Flow in the Nozzle)

In order to splat against the surface of a deflector, the water enters at an angle of 90 degrees with respect to the air flow. Splashes are further separated and accelerated as they travel along a mixing chamber toward the exit due to shear forces exerted by the air stream as they pass through it. In order to describe the internal flow in the nozzle, the VOF approach was employed since it has a conservative formulation and allows for the direct calculation of a solution without discontinuities [74,95]. It is utilized as a marker function in this method to determine how much secondary phase (liquid) is present. Since both phases have the same velocity field, the interface kinematic boundary condition is immediately satisfied. Through the use of a Dirac's delta function, the normal stress jump condition of surface tension is introduced as a source term into the momentum equation [95]. The CSF model has been used to simulate the surface tension's normal stress jump condition. In this

study, surface tension is viewed as a three-dimensional continuous influence across the interface, rather than as a boundary condition at the interface.

Among the numerous schemes available in Fluent for face flow calculation in VOF, the Euler Implicit has been selected as the steady solution. It is important to note that this approach applies the same interpolation treatment to all cells, regardless of whether they contain one or multiple phases. The term gravitational force has been introduced as a new source term. It is possible to combine the Standard k- ϵ formulation near the wall with a modified k- ϵ model in the far field using the k- SST model [96]. In this case, the Reynolds numbers for the water entrance nozzle were computed as 14,425, and the k- SST was used to calculate internal flow at both the inner and outer layers because it is more accurate and requires less computation time. Due to its approach, the model is valid throughout the near-wall zone as long as the mesh resolution is enough, and so no specific near-wall modeling is necessary, which saves time and money. The mathematical model was solved using the commercial CFD code Fluent V.2020.R1, which is available for purchase online. The SIMPLE method [97] was employed to handle the pressure–velocity coupling problem.

2.9.2. Section 2 (Flow Development)

This entails developing the flow outside the nozzle and determining the liquid's breakup length, or the point at which droplets begin to form: the primary breakup of the liquid jet near the atomizer exit and the subsequent secondary breakup of the arbitrary shaped liquid ligaments, as well as the large droplets generated from the primary breakup further downstream. The primary phase of breakup occurs near the nozzle's tip. The cavitation bubbles formed inside the nozzle, in essence, cause primary breakup, forcing the liquid to disintegrate into ligaments and large droplets. Using the empirical correlation for air blast nozzle, the primary breakup length was estimated. In this case, the Reynolds and Weber numbers were calculated at a fixed reference point near the nozzle outlet tip, and the corresponding empirical correlation was used to calculate the breakup length. The VOF method was used to develop the flow from the nozzle outlet to the breakup length.

2.9.3. Section 3 (Droplets Generation)

At the primary breakup point, droplets begin to form. The droplets travel away from the nozzle, and the gas-liquid interface becomes unstable due to the velocity difference at the shear layer of the liquid jet, to the point where viscous forces do not dampen the instabilities. Secondary breakup occurs when the instability overcomes the surface tension forces and disintegrates the liquid. The velocity profile at breakup length was extracted and used as one of the injection data for the droplet distribution to generate the droplets. The Nukiyama-Tanasawa (NT) droplet distribution method was used, and because it is not available in the ANSYS Fluent software, the STAR CCM+ software was used. The VOF—DPM approach in ANSYS Fluent used an explicit solver with a time step of 1×10^{-5} s and 7.5 million cells in the mesh, resulting in a very long computation time of about sixty hours and yet could not produce sufficient droplets. The NT approach, on the other hand, used an implicit solver with a time step of 1×10^{-3} s and 0.25 million cells in the mesh to generate a large number of droplets in less than an hour for the same condition that was used in ANSYS Fluent. According to the STAR CCM+ manual, the method necessitates some parameters for the NT equation. The droplet sauter mean diameter was extracted from the nozzle catalogue for cool-cast nozzle [48] for each air pressure and water flow rate and was used to estimate the input for the NT equation described in the literature review section to generate the input data required for the droplet generation using the NT droplet distribution. The best fit was provided by alpha and beta values of 1.2 and 1.1, respectively. For the VOF-to-DPM transition model to be effective and produce accurate results, mesh sensitivity study is necessary to produce accurate result. The cell size used was different for each case since the droplet sizes differ at different air pressure or water flow rate. However, since the droplet sizes differ at different casting condition. The principle in [98] was applied in which the mesh size was chosen such that the DPM

volume fraction is less than 10%. The maximum droplet size from the droplets size data that was estimated using N-T equation was used to estimate the cell size.

Spray cooling is accomplished through the use of a large number of droplets, each of which is traced using the Lagrangian method. In the current study, the effect of turbulence modulation caused by interaction between spray drops and gas was modeled using the method described by [99]. The WAVE model was used for secondary droplet breakup because it is designed for high-speed injections with weber numbers greater than 100. In this case, mass is accumulated from the parent drop at a rate determined by break up time until the shed mass equals 5% of the initial parcel mass. At this point, a new parcel with a new radius is created. With the exception of radius and velocity, the new parcel has the same properties as the parent parcel. The momentum of the parent parcel is adjusted so that momentum is conserved, and the new parcel is given a component of velocity randomly selected in the plane orthogonal to the direction vector of the parent parcel. The magnitude of the velocity of the new parcel is the same as the parent parcel.

2.9.4. Section 4 (Impingement and Cooling)

The input parameter was air and droplet data from Section 3's outlet. The overall heat transfer is explained in [21] as having three different components. The droplet impingement was simulated using the wall jet model, and the cooling of the steel slab was simulated using the boiling and evaporation model. The air jet is thought to thin the liquid film via shear forces, sweep away the vapor, and reduce the vapor partial pressure above the liquid film, thereby increasing evaporation [12].

Using the Section 3 results, an injection file was created. Fifty continuous phase iterations were performed between two discrete phase iterations prior to impingement, while 300 continuous phase iterations were performed between two discrete phase iterations following droplet impingement on the slab surface. The discrete phase was simulated with particle radiation interaction, two-way coupling, stochastic collision, coalescence, and breakup models. The software package used to run all the cases was ANSYS Fluent 2020R1, with each case taking approximately 48 h to converge using 128 processors.

3. Computational Domain and Boundary Conditions

3.1. Nozzle Internal Region

The dimensions and detailed information of the internal geometry is not included in this article as they are proprietary information. Figure 2 shows the dimensional air-mist nozzle used in this study.

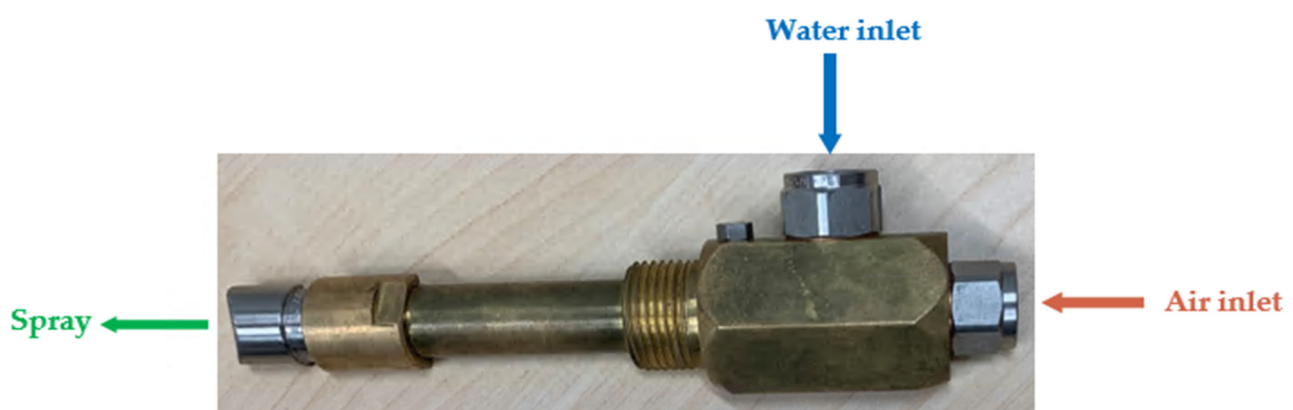


Figure 2. Air-mist nozzle model.

For Section 1 of the air-mist nozzle process, a mesh type study was considered. Figure 3a shows the front view of the nozzle with a tetrahedral mesh and indicates that an excessive cell number is obtained for the mesh transition along locations of interest. Figure 3b employs a polyhedral mesh instead, resulting in a smooth transition with fewer

cells. In both meshes, a base size of 1 mm, a total of 10 prism layers to capture flow characteristics close to the wall, a total thickness of 0.2 mm, and a transition layer ratio of 1.1 were used for the simulation.

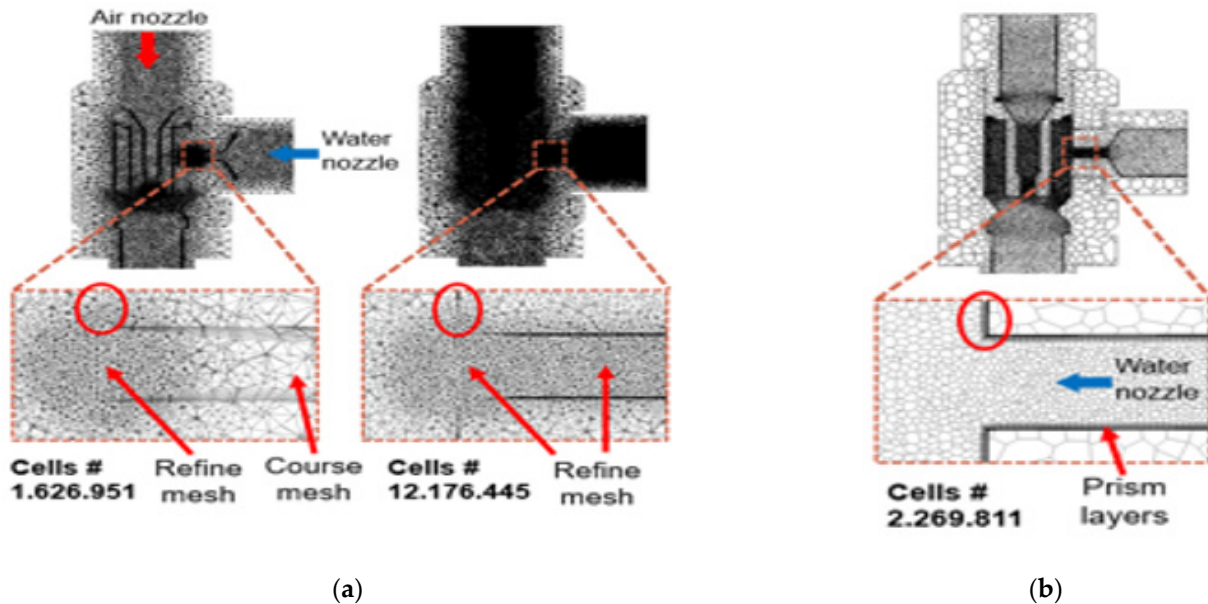


Figure 3. Nozzle meshing using (a) Tetrahedral mesh; (b) Polyhedral mesh.

The water inlet was modeled as a mass flow inlet, the air inlet as a pressure inlet, the nozzle tip outlet as pressure at 1 atm, and the nozzle walls were subjected to a non-slip condition.

Table 1 shows the casting parameters that were simulated to conduct a parametric study on the effects of air pressure, water flow rate, casting speed, and standoff distance, and to generate HTC correlation using these parameters. A 62-case matrix was generated to represent 62 different continuous casting conditions. Pseudo automatic time step was used. Air was the primary phase while water was the secondary phase and implicit VOF disperse interface model were used. Air nozzle inlet was set as pressure inlet, and the nozzle tip exit was set as pressure outlet at 1 atm. Gas properties for the compressed air phase were calculated with respect to its gage pressure. Constant fluid and gas properties were used in the simulations and a surface tension of 0.0724 N/m was set. Water inlet was modeled as mass flow inlet, the air inlet was modelled as pressure inlet, and a non-slip condition was imposed on the nozzle walls. The inlet temperature of water was maintained at 300 K in all the conditions simulated.

Table 1. Casting parameters.

Air pressure (psi)	30, 40, 45
Water flow rate (gpm)	2, 2.5, 3.7, 4.5, 6.5
Casting speed (inch/min)	40, 45, 46, 49, 50, 60
Standoff distance (inches)	5.118, 6.7, 6.89, 8.5, 12, 23, 37, 44

3.2. Spray Development

Two steps were introduced here. The first step was to validate the droplet size at 190 mm domain height. The second step was to create an external nozzle flow with the potential core length as the domain height. The air-domain dimensions were calculated using distance measurements taken during the test [100] and the flat fan air-mist nozzle characteristics. Figure 4 depicts a polyhedral mesh with a refined potential core area and a cell size of 500 μm . The potential core length downstream of the nozzle tip is 20 mm. Wake refinement with 28 degree spray angle was used to achieve the refined area. The rest of

cells size are 3 mm with growth factor of 1. The monitor plane is at 190 mm to replicate the condition in the measurement for validation of the droplet size.

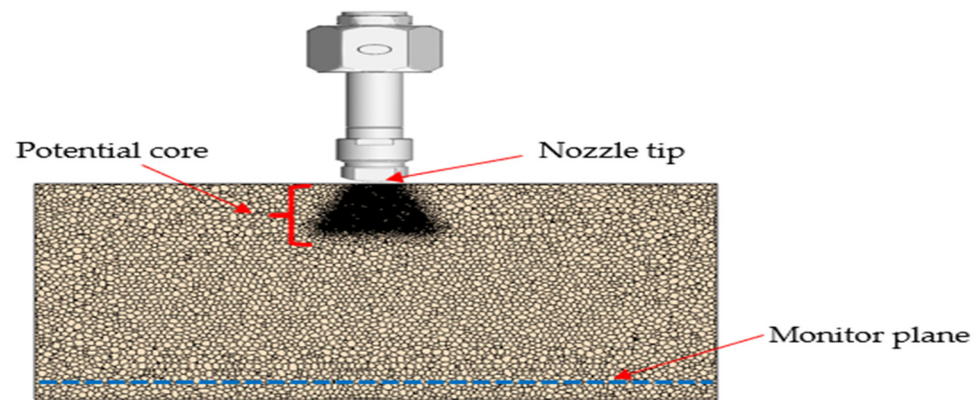


Figure 4. Polyhedral mesh for validation and spray development.

Surface tension between water liquid and gases was set as 0.0724 N/m. Implicit, sharp interface, VOF-Compressive for the volume fraction and SIMPLE scheme for the pressure-velocity coupling were used for the simulation using a time step of 1×10^{-3} s. K-omega SST viscosity model was used. The velocity profile and the water volume fraction at the outlet tip of the nozzle in section was used as the inlet condition.

3.3. Droplets Generation

Figure 5 depicts a polyhedral mesh that has been refined at the top flat fan spray pattern. The domain height varies depending on the case because breakup lengths vary, but it is measured from the breakup length to 40 mm above the slab. A 3 mm cell size was used, with 5 prism layers. At the injection surface, different cell sizes were used to refine the injection surface based on the maximum droplet size in each case.

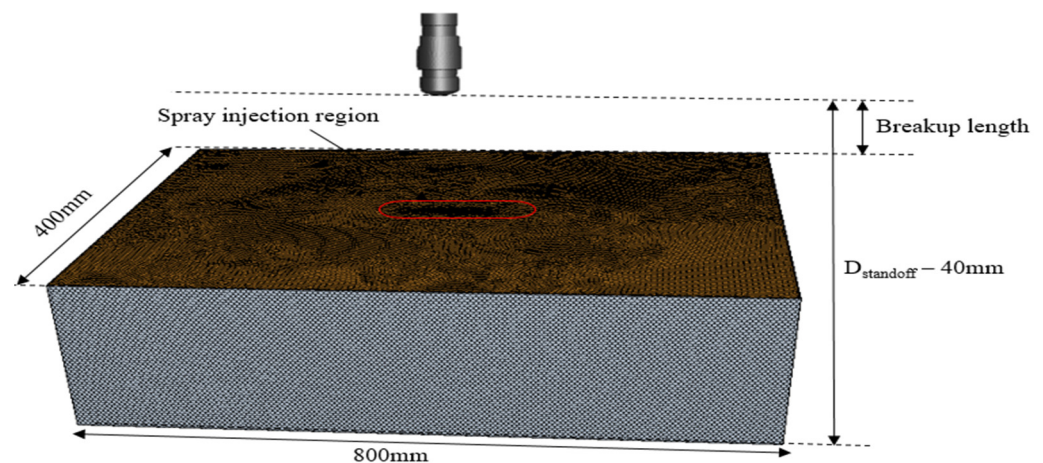


Figure 5. Computational mesh for droplets generation.

Eulerian—Lagrangian approach was used with air as the continuous phase and the water droplet as the Lagrangian phase. The NT method was used for the droplet size distribution. KHRT breakup model, turbulent dispersion, two-way coupling, pressure gradient, and drag forces were used to simulate the Lagrangian phase. The simulation was run at steady state condition using SST (Menter) K-Omega viscosity model.

3.4. Impingement and Cooling

The computational mesh used in this section is depicted in Figure 6. The cell size was chosen so that the DPM volume fraction was less than 10%. As a result, in each case, the

cell size is determined by the maximum droplet size. The slab is $800 \times 400 \times 30$ inches in size (mm). In all instances, the spray domain height is 40 mm.

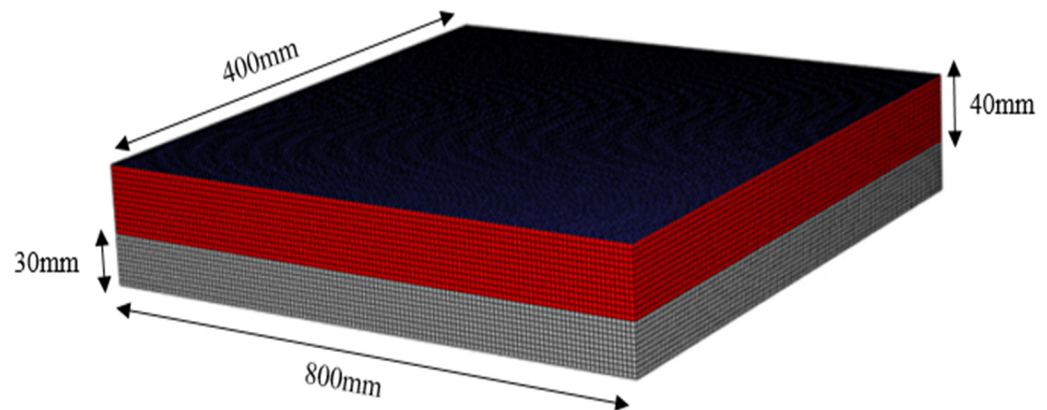


Figure 6. Structured mesh for the impingement and cooling.

The slab is moving at the speed of casting. The velocity inlet was used for air, while the pressure outlet was used for the spray domain's sides. At the slab's bottom, a symmetry condition was used. The temperature on the upstream side of the moving slab in the casting direction was set to 1473 K to represent the average temperature of the steel at the start of the secondary cooling zone. Since the temperature of the cells on the downstream side is unknown, the temperature of the cells on the downstream side is mapped to the surface using a user-defined function. The remaining slab sides are modeled as adiabatic because no heat loss is assumed. At 1473 K, the steel properties were evaluated, and these, as well as the air properties, were set as constants. The k-SST viscous model, species transport, energy, and radiation models were all employed. Using the Section 3 results, an injection file was created. Fifty continuous phase iterations were performed between two discrete phase iterations prior to impingement, while 500 continuous phase iterations were performed between two discrete phase iterations following droplet impingement on the slab surface. The discrete phase was simulated using particle radiation interaction, two-way coupling, stochastic collision, coalescence, and breakup models. ANSYS Fluent 2020R1 is the software package that was used to run all the cases.

4. Results and Discussion

4.1. Validation of Droplet Size

Air pressure of 30 psig and water flow rate 4.5 gpm was simulated for the droplets size validation. Simulated droplets measurements were taken on the same monitor plane as the test, about 190 mm from the nozzle tip as shown in Figure 7. The results validated well against the experiment in [100] where the error in measurement was about 10%.

4.2. Validation of VOF-to-DPM Model

The computational domain and boundary conditions reported by Xiaoyi et al. [101] were used for a cross-simulation to validate the VOF-to-DPM transition model. A mesh resolution of $128 \times 64 \times 64$ nodes with 5 levels of cell refinement was used to obtain a cell size of $12.5 \mu\text{m}$ which was ideal for the validation. A liquid film and ligaments breakup can be seen in Figure 8. The strong airstream at high velocity magnitude pushes the liquid injection causing it to atomize. Atomization process starts from the liquid film being pushed and distorted downstream because of air phase presence.

As result, these distortions create liquid lumps or ligaments that later will be transformed to droplets. The result validated well against the experiment result in [102].

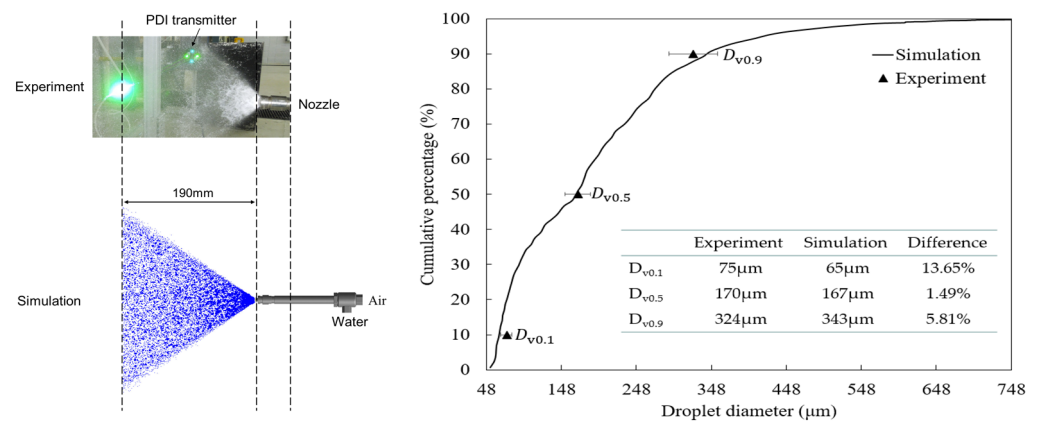


Figure 7. Validation of the droplet size.

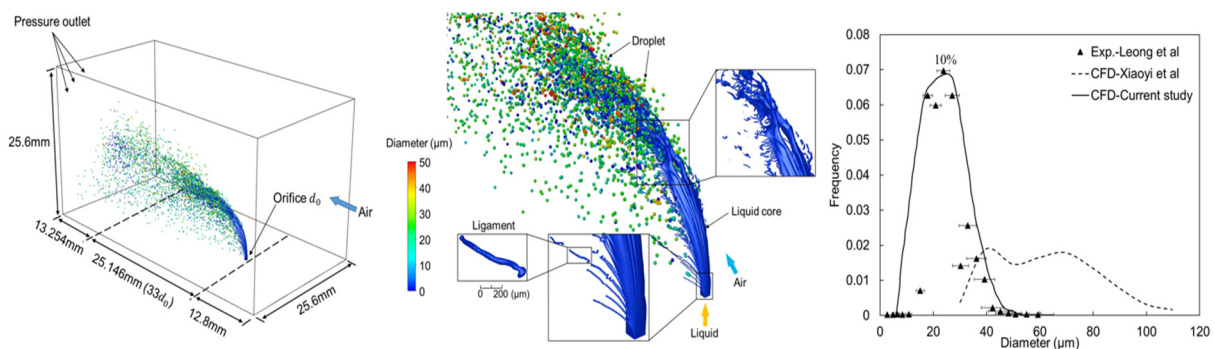


Figure 8. Validation of the VOF-DPM model.

4.2.1. Spray Cooling Result

Figure 9 shows an overlapped result of the different step. It could be seen that flat fan shaped spray pattern was generated in the third step. Some results in each step would be shown to illustrate the air-mist spray features at different casting conditions. Considering that a lot of casting conditions were simulated to generate the HTC correlation, only few of the conditions would be shown to describe the effect of changing the casting conditions.

Figure 10 depicts the results for the velocity magnitude contour and water volume fraction of water in the nozzle. An increase in air pressure causes an increase in kinetic energy, as well as an increase in the aerodynamic interaction between air and water. The increased kinetic energy is infused into the velocity, reducing surface tension forces. As a result, the water volume is reduced and the velocity is increased. As a result, the air nozzle pressure conditions have a significant impact on the degree of atomization of the liquid inside the nozzle.

When the flow rate of water increases, the volume fraction of water increases and the velocity decreases. This is due to the fact that as the flow rate of water increases, the concentration of water increases, as does the mass flux of water, resulting in an increase in frictional pressure gradient and thus a higher total pressure drop, resulting in lower velocity. Using the empirical correlation for air-blast nozzles [51], the flow properties at the nozzle tip were evaluated to estimate the breakup length. Table 2 summarizes some of the flow property results and the estimated breakup lengths. The average weber number and Reynolds number decreased as the water flow rate increased for the same air pressure, which can also be related to the decrease in velocity. The weber number and the Reynolds number are both directly proportional to velocity. As a result, the fluid is less unstable, and the breakup length is longer.

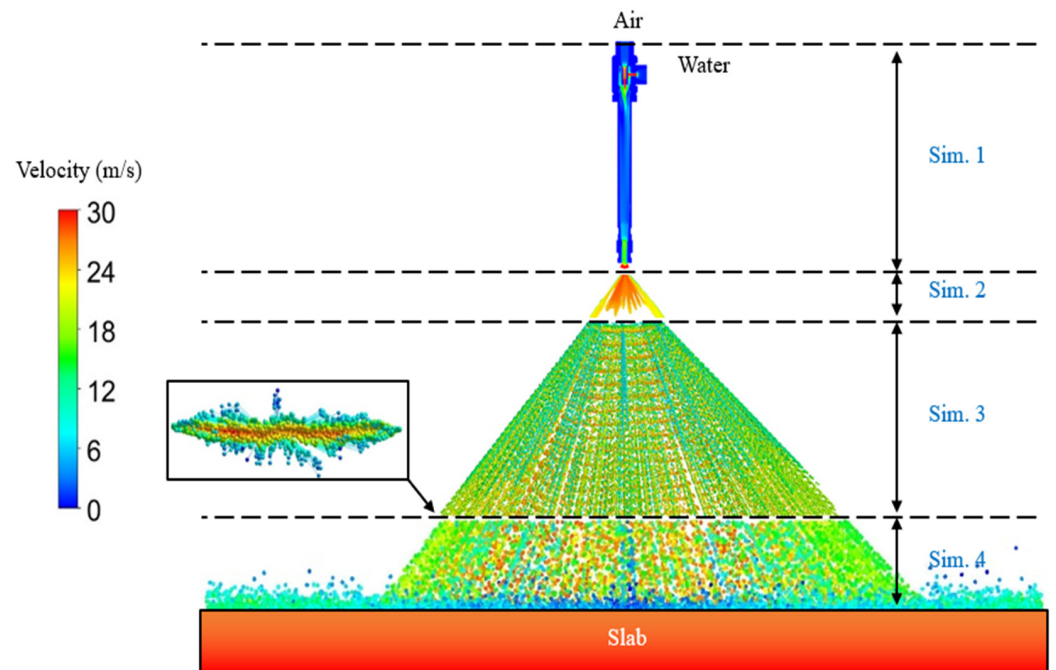


Figure 9. Overlap of the simulation results.

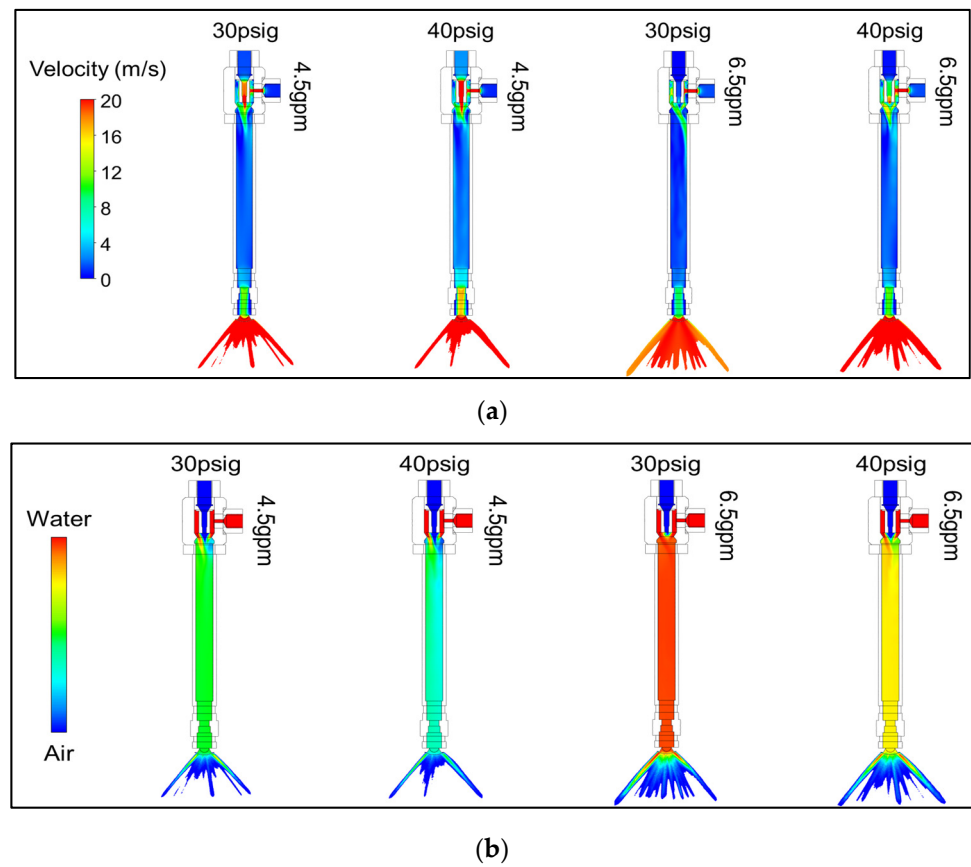


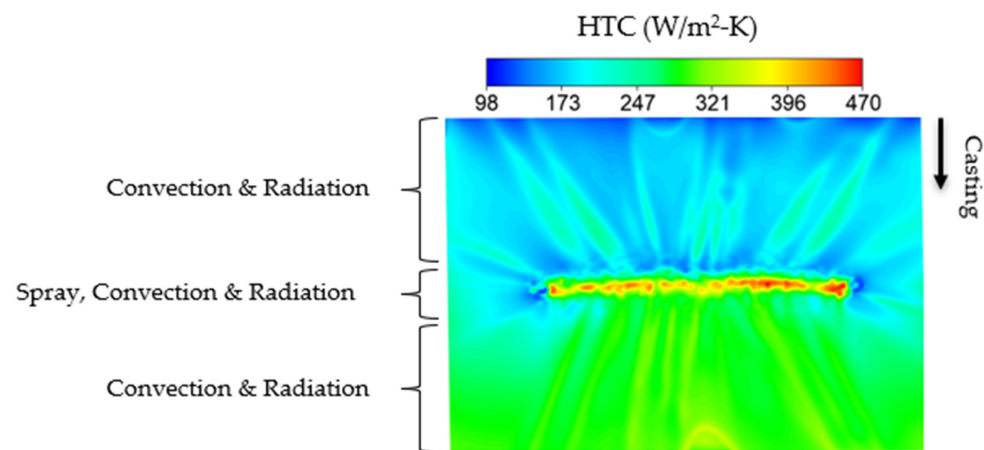
Figure 10. Cross section of nozzle tip showing (a) water VOF (b) velocity magnitude.

Table 2. Conditions at the reference line of the nozzle.

Air Pressure (psi)	Water Flow Rate (gpm)	Ave. Weber Number	Ave. Reynolds Number	Breakup Length (mm)
30	2	76.079	1083.681	14.565
30	2.5	50.381	803.261	14.845
30	3.7	41.295	556.486	15.412
40	2	116.523	1372.402	13.866
40	2.5	73.316	828.161	13.013
40	3.7	50.725	782.182	13.399
45	2	139.986	1494.343	14.316

When the air pressure was increased for the same water flow rate, the average weber number and Reynolds number increased, resulting in increased instabilities in the fluid and a shorter breakup length. This is consistent with the explanation in [96] that the shear layer causes flow instability at higher Reynolds numbers. As the weber number, which relates kinetic energy and surface tension, rises, the droplets gain more kinetic energy, which is much higher than the surface tension, causing greater instability and sheet breakup at shorter travel distances.

Droplets fall and collide with the hot steel slab surface, eventually cooling it. Figure 11 depicts a typical cooling effect on the steel slab. Water is sprayed into the roll gap, which is the space between two successive rollers, during the casting process. The non-spray region of the slab, on the other hand, retains the spray cooling effect via convection and radiation. The spray and casting parameters influence the degree and uniformity of slab cooling.

**Figure 11.** Cooling effect of the steel slab.

Two cases at (30 psi air pressure/2 gpm water flow rate and 40 psi air pressure/2 gpm water flow rate) were used to analyze the particle Stokes and Reynolds number and is shown in Table 3.

Table 3. Average particle Stokes and Reynolds number.

	$\epsilon(\text{m}^2/\text{s}^3)$		η (m)		St.		Re	
	30 psi	40 psi	30 psi	40 psi	30 psi	40 psi	30 psi	40 psi
On slab	643	761	4.69×10^{-5}	4.50×10^{-5}	8700	7205	5850	7082
10 mm above slab	59	56	8.64×10^{-5}	8.61×10^{-5}	444	482	1309	2189
30 mm above slab	42	16	9.42×10^{-5}	1.17×10^{-4}	578	360	1655	1413

As stated by many researchers [7,42,43,60,66,69,103], a typical two-phase gas-liquid atomization process has the dominant forces of hydrodynamic or inertial force attributed to undulations/perturbations, aerodynamic force attributed to drag/shearing effect, viscous force attributed to oppose a change in liquid geometry, and surface tension forces attributed to a minimum surface energy. Although particle inertia can be characterized by the Stokes number, its significance in spray atomization and transport has not been reported in any literature. It can be seen that the droplets' Stokes number as well as Reynolds number are very high. The values reported in [24,29,31,34,38] for monodisperse and bidisperse particles which had impact on particle inertia, dispersion, dissipation, and preferential accumulation were less than 400 for Reynolds number and less than 10 for the Stokes number. Although particle inertia can be characterized by the Stokes number, the Weber number associated with the normal-collision velocity is the most accurate way to characterize the impact or deformation mode of the drops, according to consensus [51,52].

4.2.2. Effect of Air Pressure on Slab Cooling

Figure 12a shows the plots of the steel slab surface temperature. To visualize the effect of air pressure, the droplets velocity and diameter after impingement on the slab is shown in Figure 12b,c respectively. These plots were at a constant water flow rate of 2 gpm and at 8.5 inches' standoff distance. It is pertinent to state that droplets exhibit different behavior upon impingement as mentioned earlier.

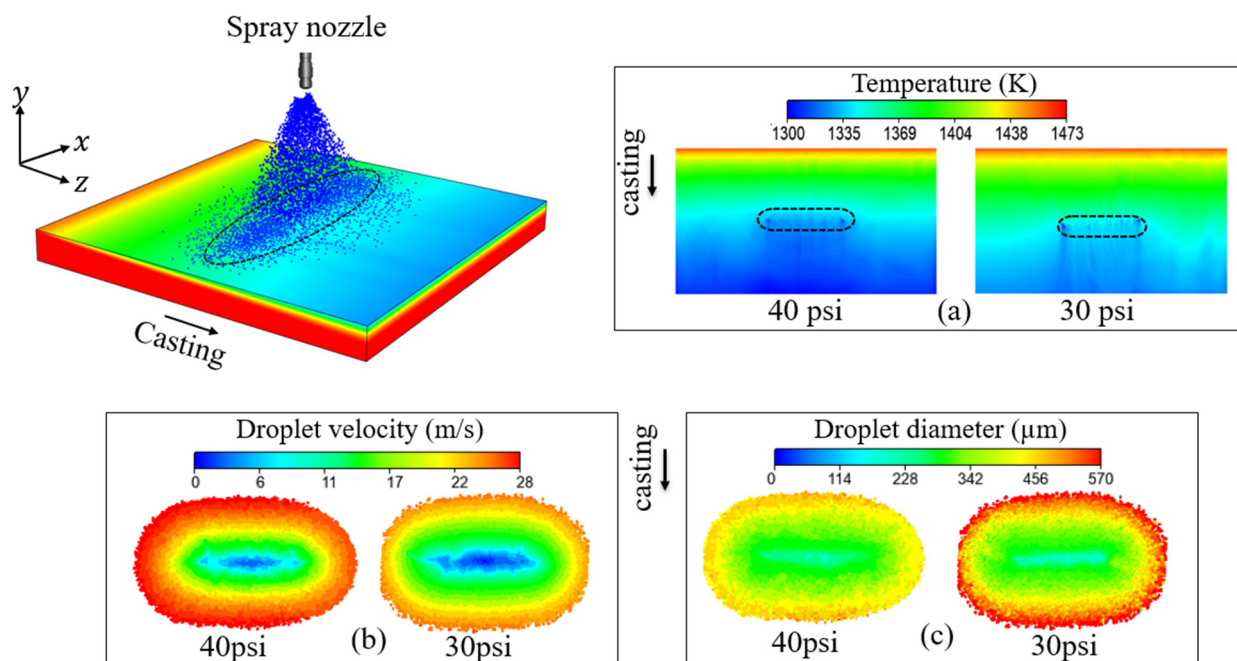


Figure 12. Sab surface contour of (a) temperature; (b) droplets velocity; (c) droplets diameter.

A closer look at the droplet diameter showed the trend explained by [103] that finer drops usually occupy the jet center and coarser drops at the border possibly due to the intersections of the crosswise streams of water and air at the entrance of the mixing chamber in this type of nozzle. It was further explained that this method of mixing cause some swirling in the drops produced with the consequent segregation of the larger ones at the periphery of the mixing chamber.

As discussed previously, the air-nozzle pressure conditions have a large effect on the degree of atomization of the liquid inside the nozzle such that fine droplets are produced. It was observed that the maximum droplet diameter on the steel slab decreased from 625 μm to 521 μm when the air pressure was increased from 30 psi to 40 psi which represents about 17% reduction in maximum droplet size. Although some percentages of the foggy drops

are blown away by the free stream air or are evaporated before reaching the steel slab, very significant number of fine drops do reach the slab at high speed. As the small droplets have large surface area to volume ratio, they will extract more heat. The visualization done by [20] revealed that interactions of the droplets with the surface are more intense at higher air nozzle pressure which suggests that a very rapid evaporation must occur. An increase in air pressure from 30 psi to 40 psi resulted in an increase in HTC as there is higher heat removal. This is because the increase in air pressure increased the droplet velocity and reduced the droplet size thus, the droplets have higher momentum to penetrate the vapor layer formed above the slab surface due to leidenfrost effect and higher kinetic energy which is a key parameter governing the higher heat extraction above the leidenfrost temperature as opined by [56]. This effect agrees with the reports of [12,21,99,103]. Table 4 shows the averaged properties of the droplets on the steel slab.

Table 4. Average droplets properties on the slab at 2 gpm water flow rate.

Droplets Properties	Unit	30 psi Air	40 psi Air
Droplets coverage area	m ²	0.0623	0.0867
Droplets weber number	-	1522	1660
Sauter mean diameter	μm	439	381
Droplets concentration	Kg/m ³	0.9854	0.4278
Droplets volume fraction	-	9.87×10^{-4}	4.29×10^{-4}
Droplets Number density	Number/m ³	4.85×10^7	2.29×10^7

Evaluation of the droplets properties on the slab surface showed that the droplets concentration on the slab decreases at higher air pressure as smaller droplets produced by increasing the air pressure could be carried away by the entrained free stream air or could evaporate before reaching the slab. For the condition evaluated in Table 3, there was about 57% reduction in the droplet concentration on the slab when the air pressure was increased from 30 psi to 40 psi. The space covered by the impinging and reflected droplets has an elliptical shape and its area was calculated where it was seen that increasing the air pressure from 30 psi to 40 psi resulted in about 39% increase in the droplets coverage area on the steel slab. It was generally agreed in [51,52,91] that the one factor governing the impact and deformation mode of the drops is the ratio of the inertial to surface tension forces of the drops given by the weber number associated with the normal collision velocity of the drops. The results shown in Table 3 also supports that increasing the air pressure from 30 psi to 40 psi at a constant water flow rate of 2 gpm increases the average droplets weber number on the steel slab by 9.1%. The droplets-to-droplets collision rate as well as the droplets number density, that is, the number of droplet particles per unit cell volume were found to both decrease as the air pressure increases. The uniformity of the spray cooling obtained by evaluating the standard deviation in the localized heat transfer coefficient showed that increase in air pressure results in more uniform cooling of the slab.

4.2.3. Effect of Water Flow Rate

An increase in the water flow rate from 2 gpm to 3.7 gpm results in lower cooling. As presented by [100], an increase in water flow rate at constant pressure imposes larger resistance on the air in the nozzle flow due to reduction in the cross-sectional area available for its flow and from the greater irreversible work it has to do for atomizing and accelerating an increasing amount of water. This result in ineffective atomization producing larger droplets size and lower velocity. This lower velocity limits the droplet—slab contact as the droplet momentum is lower and inadequate to penetrate the vapor layer above the slab surface. This is in tandem with the report in [21,100,103].

As reported by [101], increase in water flow rate at constant air pressure generally would decrease the spray cooling effectiveness because the droplets upon impinging the

hot steel slab surface, do not evaporate effectively because of the hindrance by the liquid remains from the previous drops that also evaporated partially.

4.2.4. Effect of Casting Speed

Two cases at constant air pressure of 40 psi and water flow rate of 2 gpm are shown in Figure 13 to illustrate the impact of casting speed on slab cooling. An increase in casting speed results in lower contact time between the slab and the droplets thus, lower cooling effect. The casting speed has negligible effect on the impinging and reflecting droplets velocity and sauter mean diameter on the slab. However, it was observed that the collision rate increases with casting speed resulting in relatively higher droplet number density on the slab. The discrete phase evaporation rate which measures the exchange of mass due to droplet-particle evaporation, was found to increase as the casting speed decreases.

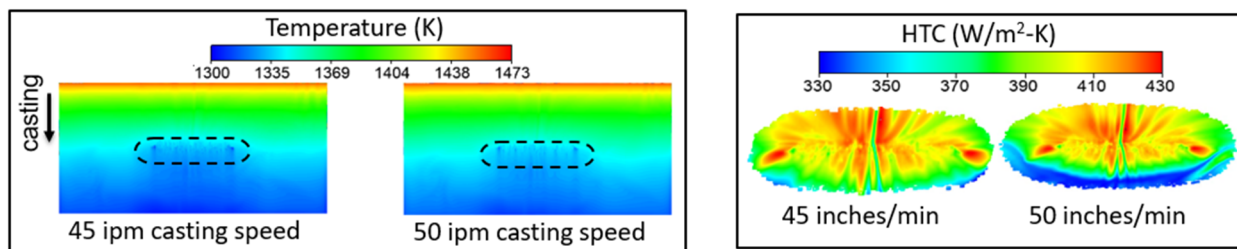


Figure 13. Slab cooling profile at 40 psi air & 2 gpm water.

4.2.5. Effect of Standoff Distance

Figure 14 shows the contour of droplets velocity and the temperature at the steel slab surface at different spray standoff distance. As the standoff distance increases for the same air pressure and water flow rate, the spray area becomes wider as the higher travel distance enables more droplets collision and coalescence that could produce finer droplets but the droplets concentration decreases as more droplets are lost either by evaporation or are being carried away by the free stream air.

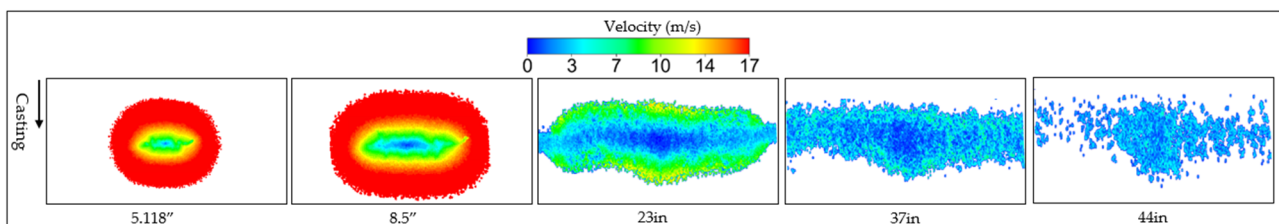


Figure 14. Contour of droplets distribution.

Also, with increase in the standoff distance, the droplets loses its kinetic energy and so the droplets velocity decreases resulting in lower cooling. However, an increase from 5.118'' to 6.7'' showed a better heat removal as the number of droplets and the spray coverage area increase with a very minimal decrease in droplets velocity but upon increasing the distance to 8.5'', the heat transfer coefficient decreased. It was also observed that as the standoff distance increases, the slab surface temperature difference decreases while the spray uniformity improves with the spray cooling having a standard deviation of 27.9 K for the 5.118 inches standoff distance and 12.2 K for the 44 inches standoff distance.

The essential standoff distance for each type of nozzle was discovered in an insightful investigation [104]. It is the absolute minimum standoff distance required for successful cooling, regardless of the water's mass flow rate. As long as the goal slab temperature is met, increasing the spray standoff distance within the critical standoff distance is encouraged. The total number of nozzles required for a continuous caster decreases as the spray cooling coverage below each nozzle grows, and a steel mill can save a significant amount of money

on nozzles as a result. When a spray nozzle is put at a distance greater than the crucial standoff distance, however, the cooling effect is barely evident. Droplet size decreases considerably at a large spray standoff distance, according to the current study. If they can land on the slab surface, smaller droplets do assist spray cooling due to their high surface to volume ratio. To put it another way, droplets must avoid being whisked away by entrained air and maintain sufficient speed after breaking up to penetrate the vapor layer floating over the slab surface.

4.2.6. Heat Transfer Coefficient Correlation

HTC is a localized parameter whose value varies depending on the casting and transversal directions. HTC values were determined using the approach described in [60]. Either linear regression analysis or curve fitting can be used to determine the relationship between the characteristic HTC and the four operating parameters. However, the final form of the correlation should be mathematically simple; otherwise, it will take a long time to compute, causing the casting control to be delayed. The simplest correlation is to suppose that the typical HTC, or aggregated HTC, is an explicit linear function of the operational parameters [60]:

$$HTC_{lump} = X_0 + X_1P_{air} + X_2Q_{water} + X_3V_{casting} + X_4D_{standoff} \quad (21)$$

where P_{air} is air pressure (psi), Q_{water} is water flow rate (l/min), $V_{casting}$ is casting speed (m/min) and $D_{standoff}$ is the standoff distance (inches). The coefficients in Equation (21) can be found through multivariable linear regression analysis. The final form of the multivariable linear regression-based correlation is shown as follows:

$$HTC_{lump} = 430.794 + 0.713P_{air} - 1.648Q_{water} - 25.623V_{casting} - 0.627D_{standoff} \quad (22)$$

Figure 15 shows the comparison between the CFD-predicted HTCs and the correlation-predicted HTCs. The multivariable linear correlation has an average error of 2.03%. The plot shows that the multivariable correlation is very accurate at predicting the CFD heat transfer coefficient. The correlation involves three basic mathematic operations, i.e., multiplication, addition, and subtraction. Such features should allow fast prediction, thereby enabling real-time casting control.

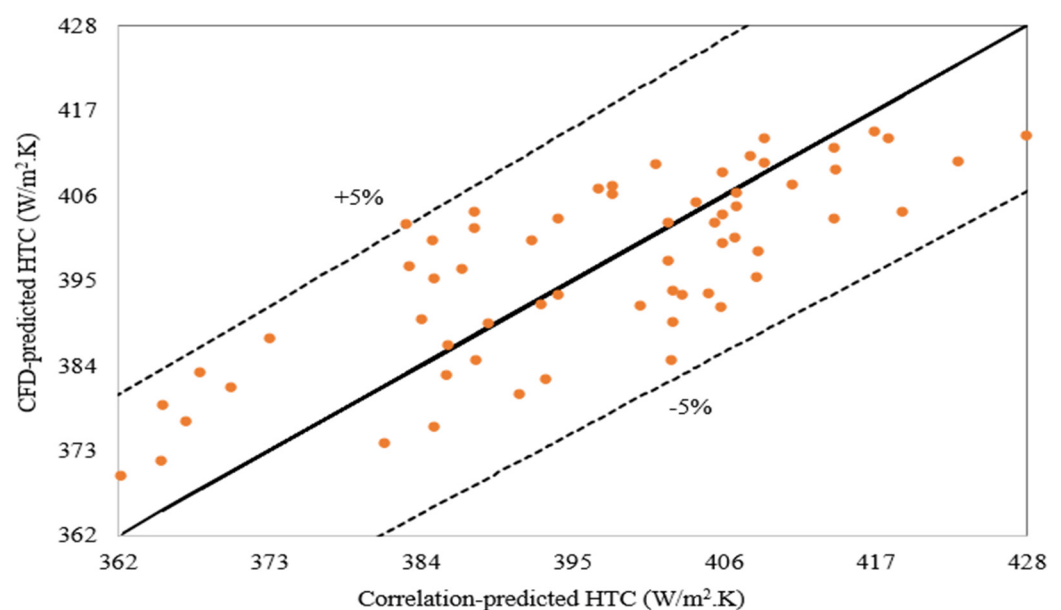


Figure 15. Parity plot of CFD and correlation predicted HTC.

When spray characteristics change, the current numerical technique should considerably minimize the time it takes to build new correlations. Furthermore, demand for new types of steel products is rapidly expanding. Each type of steel necessitates a different spray cooling approach, which includes nozzle type (hydraulic or air-mist), nozzle placement, and spray intensity (spray flow rate and standoff distance). The present high-performance computer-aided numerical method can be used to quickly create new cooling strategies.

5. Conclusions

The study numerically investigated air-mist spray cooling by a Spraying System Co. flat-fan nozzle during the secondary cooling in continuous casting of steel using a three-dimensional computational fluid dynamics simulation. The results have shown that the casting conditions have impact on the heat transfer during continuous casting of steel. A multivariable linear regression has been used to develop a correlation to predict the heat transfer coefficient using casting conditions such as air pressure, water flow rate, casting speed, and standoff distance. The following conclusions can be drawn from the results of this study:

- Increase in air pressure increases the instabilities in the water nozzle resulting in faster breakup of water; the increased air pressure also impacts on the kinetic energy of the droplets and formation of smaller droplets that ultimately improves cooling. By increasing the air pressure from 30 psi to 40 psi, the droplets size could be reduced by 17% while the droplet velocity could be increased by 27.9%. This would result in an increase in the lumped HTC by 9.2%. This effect would be more if the air pressure is increased further although there is a risk of reduced cooling effect as the very small droplets produced upon further increase could evaporate before reaching the slab thereby reducing drastically the quantity of droplets available to cool the slab.
- Increase in air pressure could also lead to droplet loss due to air entrainment or the droplets evaporating before reaching the hot steel slab if the droplet size is very small.
- With increased water flow rate from 2 gpm to 2.5 gpm at a constant air pressure of 30 psi, the weber number and Reynolds number at the nozzle outlet reduces by 33.8% and 25.9%, respectively. Increase in water flow rate increases the number of droplets on the slab but the droplets have lower velocity and higher size resulting in lower cooling of the slab.
- Increase in casting speed results in lower contact time between the droplets and the slab and thus lower cooling of the slab. At an air pressure of 40 psi and a water flow rate of 2 gpm, the cooling of the slab could decrease by 4.41% when the casting is increased from 45 ipm to 50 ipm and by 10.29% when it is further increased to 60 ipm.

Author Contributions: V.A. conducted the CFD simulations, analyzed the data, generated the correlation and wrote the manuscript. H.M. conceptualized the methodology, provided guidance to CFD simulations, reviewed and edited the manuscript. A.S. supervised the research process, provided guidance to CFD simulations, and reviewed and edited the manuscript. C.Z. acquired funding for the current study, supervised the research process, and reviewed and edited the manuscript. All authors have read and agreed to the published version of the manuscript.

Funding: This work was funded by the Steel Manufacturing Simulation and Visualization Consortium (SMSVC).

Data Availability Statement: The original contributions presented in the study are included in the article, further inquiries can be directed to the corresponding authors.

Acknowledgments: The authors would like to thank the Steel Manufacturing Simulation and Visualization Consortium (SMSVC) members for funding this project. The Center for Innovation through Visualization and Simulation (CIVS) at Purdue University Northwest is well appreciated for providing all the resources required for this work.

Conflicts of Interest: The authors declare no conflict of interest.

References

1. Laitinen, E.; Neittaanmaaki, P. On Numerical Simulation of the Continuous Casting Process. *J. Eng. Math.* **2003**, *22*, 335–354. [[CrossRef](#)]
2. Thomas, B.G. Continuous Casting (metallurgy). In *Yearbook of Science and Technology*; McGraw-Hill Co.: New York, NY, USA, 2004.
3. Stahl: World Steel Production. 2009. Available online: http://www.stahlonline.de/english/business_and_politics/economic_and_trade_policy/steel_in_figures/start.asp (accessed on 13 February 2020).
4. Sengupta, J.; Thomas, B.G.; Wells, M.A. The use of water cooling during the continuous casting of steel and aluminium. *Metall. Mater. Trans. B* **2005**, *36*, 187–204. [[CrossRef](#)]
5. Camporredondo, S.J.E.; Castillejos, E.A.H.; Acosta, G.F.A.; Gutierrez, M.E.P.; Herrera, G.M.A. Analysis of Thin-Slab Casting by the Compact-Strip Process: Part I. Heat Extraction and Solidification. *Metall. Mater. Trans. B* **2004**, *35*, 541–559. [[CrossRef](#)]
6. Hibbins, S.G.; Brimacombe, J.K. Characterization of heat transfer in the secondary cooling system of a continuous slab caster. *ISS Trans.* **1983**, *3*, 77–89.
7. Haibo, M.; Justina, L.; Kaile, T.; Rui, L.; Michael, L.; Armin, S.; Chenn, Q.Z. Modelling of spray cooling with a moving steel slab during the continuous casting process. *Steel Res. Int.* **2019**, *90*, 18000393.
8. Visaria, M.; Issam, M. Theoretical and experimental study of the effects of spray inclination on two-phase spray cooling and critical heat flux. *Int. J. Heat Mass Transfer* **2008**, *51*, 2398. [[CrossRef](#)]
9. Mitsutake, Y.; Monde, M.J. Analytical method of two-dimensional inverse heat conduction problem using Laplace transformation: Effect of number of measurement point. *Heat Transfer* **2003**, *125*, 6.
10. Mozumder, A.K.; Monde, M.; Woodfield, P.L.; Islam, M.A. Maximum heat flux in relation to quenching of a high temperature surface with liquid jet impingement. *Int. J. Heat Mass Transfer* **2006**, *49*, 2877. [[CrossRef](#)]
11. Moravec, R.; Blazek, K.; Horsky, J.; Graham, J.; Fiegle, S.; Dombovic, T.; Kaurich, T. Coupling of Solidification model and Heat Transfer Coefficients to have Valuable Tool for Slab Surface Temperatures Prediction. In Proceedings of the T in METEC InSteelCon, Düsseldorf, Germany, 27 June–1 July 2011.
12. Kim, J. Spray cooling heat transfer: The state of the art. *Int. J. Heat Fluid Flow* **2007**, *28*, 753–767. [[CrossRef](#)]
13. Nitin, K.; Tatiana, G.R.; Peter, S.; Cam, T. A hydrodynamic model for subcooled liquid jet impingement at the Leidenfrost condition. *Int. J. Therm. Sci.* **2011**, *50*, 993–1000.
14. Müller, H.; Jeschar, R. Untersuchung des Wärmeübergangs an einer simulierten Sekundärkühlzone beim Stranggießverfahren. *Arch. Eisenhüttenwesen* **1978**, *44*, 589–594. [[CrossRef](#)]
15. Choi, K.J.; Yao, S.C. Mechanisms of film boiling heat transfer of normally impacting spray. *Int. J. Heat Mass Transf.* **1987**, *30*, 311–318. [[CrossRef](#)]
16. Deb, S.; Yao, S.C. Analysis on film boiling heat transfer of impacting sprays. *Int. J. Heat Mass Transf.* **1989**, *32*, 2099–2112. [[CrossRef](#)]
17. Fujimoto, H.; Hatta, N.; Asakawa, H.; Hashimoto, T. Predictable Modelling of Heat Transfer Coefficient between Spraying Water and a Hot Surface above the Leidenfrost Temperature. *ISIJ Int.* **1997**, *37*, 492–497. [[CrossRef](#)]
18. Horsky, J.; Raudensky, M.; Tseng, A.A. Heat transfer study of secondary cooling in continuous casting. In Proceedings of the AISTech 2005, Iron & Steel Technology Conference and Exposition, Charlotte, NC, USA, 9–12 May 2005.
19. Hernández, B.A.; Minchaca, M.J.I.; Castillejos, E.A.H.; Acosta, G.F.A.; Xiaoxu, Z.; Thomas, B.G. Measurement of heat flux in dense air-mist cooling: Part II—The influence of mist characteristics on steady-state heat transfer. *Exp. Therm. Fluid Sci.* **2013**, *44*, 161–173. [[CrossRef](#)]
20. Mario, E.H.L.; Esther, M.G.M.; Castillejos, E.A.H. Heat Transfer and Observation of Droplet-Surface Interactions During Air-Mist Cooling at CSP Secondary System Temperatures. *Metall. Mater. Trans. B* **2016**, *47*, 1409.
21. Mishra, P.C.; Nayak, S.K.; Pradhan, P.; Durga, P.G. Impingement Cooling of Hot Metal Strips in Runout Table—A Review. *Interfac. Phenom. Heat Transfer* **2015**, *3*, 117–137. [[CrossRef](#)]
22. Gradeck, M.; Kouachi, A.; Lebouche, M.; Volle, F.; Maillat, D.; Borean, J.L. Boiling curves in relation to quenching of a high temperature moving surface with liquid jet impingement. *Int. J. Heat Mass Transf.* **2009**, *52*, 1094. [[CrossRef](#)]
23. Islam, M.A.; Monde, M.; Woodfield, P.L.; Mitsutake, Y. Jet impingement quenching phenomena for hot surfaces well above the limiting temperature for solid–liquid contact. *Int. J. Heat Mass Transf.* **2008**, *51*, 1226. [[CrossRef](#)]
24. Balachandar, S.; Eaton, J.K. Turbulent dispersed multiphase flow. *Annu. Rev. Fluid Mech.* **2010**, *42*, 111–133. [[CrossRef](#)]
25. Crowe, C.T.; Schwarzkopf, J.D.; Sommerfeld, M.; Tsuji, Y. *Multiphase Flows with Droplets and Particles*; CRC Press: Boca Raton, FL, USA, 2011.
26. Elghobashi, S. Particle-laden turbulent flows: Direct simulation and closure models. *Appl. Sci. Res.* **1991**, *48*, 301–314. [[CrossRef](#)]
27. Elghobashi, S. On predicting particle-laden turbulent flows. *Appl. Sci. Res.* **1994**, *52*, 309–329. [[CrossRef](#)]
28. Elghobashi, S.; Truesdell, G.C. Direct simulation of particle dispersion in a decaying isotropic turbulence. *J. Fluid Mech.* **1992**, *242*, 655–700. [[CrossRef](#)]
29. Maxey, M.R. The gravitational settling of aerosol particles in homogeneous turbulence and random flow fields. *J. Fluid Mech.* **1987**, *174*, 441–465. [[CrossRef](#)]
30. Squires, K.D.; Eaton, J.K. Preferential concentration of particles by turbulence. *Phys. Fluids A* **1991**, *3*, 1169–1179. [[CrossRef](#)]
31. Momenifar, M.; Dhariwal, R.; Bragg, A.D. Influence of Reynolds number on the motion of settling, bidisperse inertial particles in turbulence. *Phys. Rev. Fluids* **2019**, *4*, 054301. [[CrossRef](#)]

32. Bec, J.; Homann, H.; Ray, S.S. Gravity-Driven Enhancement of Heavy Particle Clustering in Turbulent Flow. *Phys. Rev. Lett.* **2014**, *112*, 184501. [[CrossRef](#)]
33. Ireland, P.J.; Bragg, A.D.; Collins, L.R. The effect of Reynolds number on inertial particle dynamics in isotropic turbulence. Part 2. Simulations with gravitational effects. *J. Fluid Mech.* **2016**, *796*, 659. [[CrossRef](#)]
34. Dhariwal, R.; Bragg, A.D. Enhanced and suppressed multiscale dispersion of bidisperse inertial particles due to gravity. *Phys. Rev. Fluids* **2019**, *4*, 034302. [[CrossRef](#)]
35. Zhou, Y.; Wexler, A.S.; Wang, L.P. Modelling turbulent collision of bidisperse inertial particles. *J. Fluid Mech.* **2001**, *433*, 77. [[CrossRef](#)]
36. Chen, J.; Jin, G. Large-eddy simulation of turbulent preferential concentration and collision of bidisperse heavy particles in isotropic turbulence. *Powder Technol.* **2017**, *314*, 281. [[CrossRef](#)]
37. Kruis, F.E.; Kusters, K.A. The collision rate of particles in turbulent flow. *Chem. Eng. Commun.* **1997**, *158*, 201. [[CrossRef](#)]
38. Wang, L.P.; Maxey, M.R. Settling velocity and concentration distribution of heavy particles in homogeneous isotropic turbulence. *J. Fluid Mech.* **1993**, *256*, 27. [[CrossRef](#)]
39. Bec, J.; Biferale, L.; Boffetta, G.; Celani, A.; Cencini, M.; Lanotte, A.S.; Musacchio, S.; Toschi, F. Acceleration statistics of heavy particles in turbulence. *J. Fluid Mech.* **2006**, *550*, 349. [[CrossRef](#)]
40. Ayyalasomayajula, S.; Warhaft, Z.; Collins, L.R. Modeling inertial particle acceleration statistics in isotropic turbulence. *Phys. Fluids* **2008**, *20*, 095104. [[CrossRef](#)]
41. Chang, K.; Malec, B.J.; Shaw, R.A. Turbulent pair dispersion in the presence of gravity. *New J. Phys.* **2015**, *17*, 033010. [[CrossRef](#)]
42. Alam, U.; Krol, J.; Specht, E.; Schmidt, J. Enhancement and Local Regulation of Metal Quenching Using Atomized Sprays. *J. ASTM Int.* **2008**, *5*, 91–103.
43. Lefebvre, A.H.; McDonell, V.G. *Atomization and Sprays*; CRC Press: Boca Raton, FL, USA, 2017.
44. Mitsutsuka, M.; Fukuda, K. Boiling phenomena and effects of water temperature on heat transfer in the process of immersion cooling. *Tsutsu Hagane* **1979**, *65*, 608–616. [[CrossRef](#)]
45. Mitsutsuka, M.; Fukuhisa, Y.; Wake, M.; Okajima, M.; Miyashita, N.; Takeda, Y. Development of Air-atomizing Mist Nozzles and Mist Cooling System for Continuous Casting. *Trans. ISIJ* **1985**, *25*, 1244–1250. [[CrossRef](#)]
46. Jeschar, R.; Reiners, U.; Scholz, R. Heat Transfer During Water and Water-Air Spray Cooling in the Secondary Cooling Zone of Continuous Casting Plants. In Proceedings of the 69th Steelmaking Conference, Washington, DC, USA, 6–9 April 1986; pp. 511–521.
47. Raudensky, M.; Horsky, J. Secondary cooling in continuous casting and Leidenfrost temperature effects. *Ironmak. Steelmak.* **2005**, *32*, 159–164. [[CrossRef](#)]
48. Horský, J.; Raudenský, M. Measurement of heat transfer characteristics of secondary cooling in continuous casting. *Metal* **2005**, *24*–26.5.
49. McGinnis, F.K.; Holman, J.P. Individual droplet heat-transfer rates for splattering on hot surfaces. *Int. J. Heat Mass Transf.* **1969**, *12*, 95–108. [[CrossRef](#)]
50. Pedersen, C.O. An experimental study of the dynamic behavior and heat transfer characteristics of water droplets impinging upon a heated surface. *Int. J. Heat Mass Transf.* **1970**, *13*, 369–379. [[CrossRef](#)]
51. Araki, K.; Moriyama, A. Theory on Deformation Behaviour of a Liquid Droplet Impinging onto Hot Metal Surface. *Trans. ISIJ* **1981**, *21*, 583–590. [[CrossRef](#)]
52. Wachters, L.H.J.; Westerling, N.A. The heat transfers from a hot wall to impinging mist droplets in the spheroidal state. *Chem. Eng. Sci.* **1966**, *21*, 1047–1056. [[CrossRef](#)]
53. Prinz, B.; Bamberger, M. Determination of heat transfer coefficient of air mist sprays. *Mater. Sci. Technol.* **1989**, *5*, 389–393. [[CrossRef](#)]
54. Jenkins, M.S.; Story, S.R.; Davies, R.H. Measurement and Characterisation of Air-Mist Nozzles for Spray Quenching Heat Transfer. In Proceedings of the 19th Australasian Chemical Engineering Conference, Newcastle, UK, 18–20 September 1991; pp. 161–169.
55. Puschmann, F.; Specht, E. Transient measurement of heat transfer in metal quenching with atomized sprays. *Exp. Therm. Fluid Sci.* **2004**, *28*, 607–615. [[CrossRef](#)]
56. Bendig, L.; Raudensky, M.; Horsky, J. Spray parameters and heat transfer coefficients of spray nozzles for continuous casting. In Proceedings of the Seventy-Eight Steelmaking Conference, Iron and Steel Society, Nashville, TN, USA, 2–5 April 1995; pp. 391–398.
57. Montes, R.J.J.; Castillejos, E.A.H.; Acosta, G.F.A.; Gutiérrez, M.E.P.; Herrera, G.M.A. Effect of the operating conditions of air-mists nozzles on the thermal evolution of continuously cast thin slabs. *Can. Metall. Q.* **2008**, *47*, 187–204.
58. Castillejos, E.A.H.; Acosta, G.F.A.; Herrera, M.A.; Hernández, C.I.; Gutiérrez, M.E.P. Practical productivity gains—Towards a better understanding of air-mist cooling in thin slab continuous casting. In Proceedings of the Third International Congress of Steelmaking, Association of Iron and Steel Technology, Charlotte, NC, USA, 9–12 May 2005; pp. 881–890.
59. Schmidt, J.; Boye, H. Influence of velocity and size of the droplets on the heat transfer in spray cooling. *Chem. Eng. Technol.* **2001**, *24*, 255–260. [[CrossRef](#)]
60. Haibo, M.; Armin, S.; Chenn, Z. Numerical Development of Heat Transfer Coefficient Correlation for Spray Cooling in Continuous Casting. *Front. Mater.* **2020**, *7*, 577265.

61. Mascarenhas, N.; Mudawar, I. Methodology for predicting spray quenching of thick-walled metal alloy tubes. *Int. J. Heat Mass Transfer* **2012**, *55*, 2953–2964. [[CrossRef](#)]
62. Agnieszka, C.R.; Zbigniew, M.; Andrzej, B. The influence of selected parameters of spray cooling and thermal conductivity on heat transfer coefficient. *Int. J. Therm. Sci.* **2016**, *110*, 52–64.
63. Haibo, M.; Rui, L.; Micheal, L.; Armin, S.; Chenn, Z. Numerical Investigation of Spray Cooling at Various Operation Conditions during Continuous Casting of Steel. In Proceedings of the AISTech Conference, Pittsburgh, PA, USA, 6–9 May 2019.
64. Nukiyama, S.; Tansawa, Y. Experiments on the atomization of liquids in atomized jet. *Trans. Soc. Mech. Engrs. (Japan)* **1939**, *6*, II-7, II-15.
65. Zeoli, N.; Tabbara, H.; Gu, S. CFD Modeling of Primary Breakup during Metal Powder Spray. *Chem. Eng. Sci.* **2011**, *66*, 6498–6504. [[CrossRef](#)]
66. Altimira, M.; Rivas, A.; Anton, R.; Sanchez, L.G.; Ramos, J.C. Fan-Spray Atomizers Analysis through Mathematical Modeling. In Proceedings of the ILASS-Europe Conferences, Mugla, Turkey, 10–13 September 2007.
67. Koutsakis, K.; Gu, S.; Vardelle, A. Three Dimensional CFD Simulation of Liquid Copper Break up for the Liquid Precursor Spraying. *Surf. Coat. Technol.* **2011**, *220*, 214–218. [[CrossRef](#)]
68. Kalata, W.; Brown, K.; O'Donnell, S.; Schick, R.J. Transfer Efficiency for an Oil Spray Application. In Proceedings of the 26th ILASS Americas Annual Conference on Liquid Spray and Spray Systems, Portland, OR, USA, 16–19 May 2016.
69. Alkhedhair, A.; Jahn, I.; Gurgenci, H.; Guan, Z.; He, S.; Lu, Y. Numerical Simulation of Water Spray in Natural Draft Dry Cooling Towers with a New Nozzle Representation Approach. *Appl. Therm. Eng.* **2016**, *98*, 924–935. [[CrossRef](#)]
70. Crowe, C.T.; Sharma, M.P.; Stock, D.E. The Particle-Source-In Cell (PSI-CELL) Model for Gas-Droplet Flows. *J. Fluids Eng.* **1977**, *99*, 325–332. [[CrossRef](#)]
71. Zuckerman, N.; Lior, N. Jet impingement heat transfer: Physics, correlations, and numerical modeling. *Adv. Heat Transfer* **2006**, *39*, 565.
72. Menter, F.R. Multiscale model for turbulent flows. In Proceedings of the AIAA 24th Fluid Dynamics Conference, Orlando, FL, USA, 6–9 July 1993.
73. Ishii, M. Thermo-fluid Dynamics Theory of Two-phase Flow. *Eyrolles Paris* **1975**, *75*, 29657.
74. Hirt, C.W.; Nichols, B.D. Volume of fluid (VOF) method for the dynamics of free boundaries. *J. Comp. Phys.* **1981**, *39*, 201. [[CrossRef](#)]
75. Kothe, D.B.; Mjolsness, R.C. RIPPLE: A new model for incompressible flows with free surfaces. *AIAA J.* **1992**, *30*, 2694. [[CrossRef](#)]
76. Kothe, D.B.; Rider, W.J.; Mosso, S.J.; Brock, J.I.; Hochstein, J.S. Volume tracking of interfaces having surface tension in two and three dimensions. In Proceedings of the AIAA 34th Aerospace Sciences Meeting and Exhibit, Reno, NV, USA, 15–18 January 1996. Paper 96-0859.
77. Richards, J.R.; Beris, A.N.; Lenhoff, A.M. Drop formation in liquid–liquid systems before and after jetting. *Phys. Fluids* **1995**, *7*, 2617. [[CrossRef](#)]
78. Rayleigh, L. On the instability of jets. *Proc. Lond. Math. Soc.* **1878**, *1*, 4–13. [[CrossRef](#)]
79. Reitz, R.D. Atomization and Other Breakup Regimes of a Liquid Jet. Ph.D. Thesis, Princeton University, Princeton, NJ, USA, 1978.
80. Reitz, R.D. Modeling atomization processes in high-pressure vaporizing sprays. *At. Spray Technol.* **1987**, *3*, 309–337.
81. Nijdam, J.J.; Guo, B.; Fletcher, D.F.; Langrish, T.A. Lagrangian and Eulerian models for simulating turbulent dispersion and coalescence of droplets within a spray. *Appl. Math. Model.* **2006**, *30*, 1196–1211. [[CrossRef](#)]
82. Fung, M.C.; Inthavong, K.; Yang, W.; Tu, J. CFD modeling of spray atomization for a nasal spray device. *Aerosol. Sci. Technol.* **2012**, *46*, 1219–1226. [[CrossRef](#)]
83. Eroglu, H.; Chigier, N.; Farago, Z. Coaxial atomizer liquid intact lengths. *Phys. Fluids A* **1991**, *3*, 303–308. [[CrossRef](#)]
84. Leroux, B.; Delabroy, O.; Lacas, F. Experimental study of coaxial atomizers scaling. Part I: Dense core zone. *At. Sprays* **2007**, *17*, 381–407. [[CrossRef](#)]
85. Zhao, H.; Liu, H.F.; Tian, X.S. Influence of atomizer exit area ratio on the breakup morphology of coaxial air and round water jets. *AIChE J.* **2014**, *60*, 2335–2345. [[CrossRef](#)]
86. Engelbert, C.; Hardalupas, Y.; Whitelaw, J.H. Breakup phenomena in coaxial airblast atomizers. *Proc. R. Soc. Lond. A* **1995**, *451*, 189–229.
87. Kumar, A.; Sahu, S. Liquid jet breakup unsteadiness in a coaxial air-blast atomizer. *Int. J. Spray Combust. Dyn.* **2018**, *10*, 211–230. [[CrossRef](#)]
88. O'Rourke, P.J.; Bracco, F.V. Modeling of Drop Interactions in Thick Sprays and Comparison with Experiments. *Instit. Mech. Eng.* **1980**, *404*, 80.
89. Liu, A.B.; Mather, D.; Reitz, R.D. Modeling the Effects of Drop Drag and Breakup on Fuel Sprays. *SAE Int. J. Eng.* **1993**, *102*, 83–95.
90. Ranz, W.E.; Marshall, W.R. Evaporation from Drops. *Chem. Eng. Progress* **1952**, *48*, 141–146.
91. Naber, J.D.; Reitz, R.D. Modeling Engine Spray/Wall Impingement. *SAE Int. J. Eng.* **1988**, *97*, 118–140.
92. Bernardin, J.D.; Mudawar, I. The Leidenfrost point: Experimental study and assessment of existing models. *J. Heat Trans.* **1999**, *121*, 894–903. [[CrossRef](#)]
93. Miller, R.S.; Harstad, K.; Bellan, J. Evaluation of Equilibrium and Non-Equilibrium Evaporation Models for Many Droplet Gas-Liquid Flow Simulations. *Int. J. Multiphase Flow* **1998**, *24*, 1025–1055. [[CrossRef](#)]

94. Sazhin, S.S. Advanced Models of Fuel Droplet Heating and Evaporation. *Progress Energy Combust. Sci.* **2006**, *32*, 162–214. [[CrossRef](#)]
95. Brackbill, J.U.; Kothe, D.B.; Zemach, C. A continuum method for modeling surface tension. *J. Comput. Phys.* **1992**, *100*, 335–354. [[CrossRef](#)]
96. Menter, F.R.; Kuntz, M.; Langtry, R. Ten years of experience with the SST turbulence model. *Turbul. Heat Mass Transf.* **2003**, *4*, 625–632.
97. Patankar, S.V.; Spalding, D.B. A calculation procedure for heat, mass and momentum transfer in three-dimensional parabolic flows. *Int. J. Heat Mass Transf.* **1972**, *15*, 1787. [[CrossRef](#)]
98. Jadidi, M. Introduction to Multiphase Flows-Part#2 Fundamental Definitions & Choosing a Multiphase Model. Available online: https://www.researchgate.net/publication/312228367_Introduction_to_Multiphase_Flows-Part_2_Fundamental_Definitions_Choosing_a_Multiphase_Model (accessed on 4 June 2021).
99. Reitz, R.D.; Diwakar, R. Structure of high-pressure fuel sprays. *SAE Paper* **1987**, 492–509.
100. Spray Analysis and Research Services. Spray Characterization of Nozzles Used in Casting Application. Laboratory Test Report. April 2016. Available online: <https://www.sprayanalysis.com/> (accessed on 1 November 2021).
101. Xiaoyi, L.; Marco, A.; Marcos, S.; Mark, S. Towards an efficient, high-fidelity methodology for liquid jet atomization computations. In Proceedings of the 48th Aerospace Sciences Meeting, Orlando, FL, USA, 4–7 January 2010.
102. Leong, M.Y.; Hautman, D.J. Near-field spray characterization of a liquid fuel jet injected into a crossflow. In Proceedings of the ILASS Americas, 15th Annual Conference on Liquid Atomization and Spray Systems, Madison, WI, USA, 14–17 May 2002.
103. Minchacha, M.J.L.; Castillejos, E.A.H.; Acosta, G.F.A. Size and velocity characteristics of droplets generated by thin steel slab continuous casting secondary cooling air-mist nozzles. *Metall. Mater. Trans. B* **2011**, *42*, 500–515. [[CrossRef](#)]
104. Yao, S.C.; Cox, T.L. Investigation into the Use of Large-Drop Sprays for Hot Strip Rolling Mills. In Proceedings of the Mechanical Working and Steel Processing Conference, Pittsburgh, PA, USA, 25–28 October 1998; pp. 359–366.